**The Thesis Committee for Kai Wang**
**Certifies that this is the approved version of the following thesis:**

# Evaluation of a land surface solar radiation partitioning scheme using remote sensing and site level FPAR datasets

**APPROVED BY**
**SUPERVISING COMMITTEE:**

**Supervisor:**

Robert E. Dickinson

Rong Fu

Zong-liang Yang

# Evaluation of a land surface solar radiation partitioning scheme using remote sensing and site level FPAR datasets

**by**

**Kai Wang, B.S.; M.S.**

**Thesis**

Presented to the Faculty of the Graduate School of

The University of Texas at Austin

in Partial Fulfillment

of the Requirements

for the Degree of

**Master of Science in Geological Sciences**

**The University of Texas at Austin**

**August 2013**

## Acknowledgements

Foremost, I thank my parents for their selfless love and continuous support, for always being a phone call away to talk about my life and encouraging me to face any challenges.

This thesis would not have been possible without the guidance of Dr. Robert Dickinson and Dr. Jiafu Mao. I am extremely fortunate to have been advised by such exceptional scientist who provided invaluable science discussions and tremendous support and encouragement in my research. I would like to express my sincere gratitude to my advisor, Robert Dickinson, for his support of my master study and research, for his patience, motivation, immense knowledge, and for his numerous thorough revisions of my manuscript. My sincere thanks also goes to Dr. Jiafu Mao, my advisor during internship at the Oak Ridge National Laboratory (ORNL), for his technical, intellectual and moral support on my research and developing my analytical and research skills.

Besides my advisors, I also get great help from numerous researchers. Dr. Zongliang Yang helped shape my perception of the model structure and motivated the use of remote sensing products. Dr. Lianhong Gu from ORNL greatly inspired me to look into the sun angle dependency in FPAR. Dr. Rong Fu offered insightful comments to my research. Dr. Xiaoying Shi, Dr. Mac Post and Dr. Peter E. Thornton from ORNL helped me with my research during my internship. Dr. Bing Pu offered valuable discussions and technical support. Dr. Mahammad Shaikh offered great help with software issues. Researchers including Dr. Kaicun Wang, Dr. Kerry Cook, Dr.

Ned Vizy, Dr. Dan Breecker and Dr. Tim Shanahan helped shape my scientific thought and reasoning.

I also thank my research group: Ying Sun, Wenting Fu, Lacey Pyle, Binyan Yan, Hua Yuan, Hua Su and Jamie Wentz for helping me through my graduate studies with fun and support. I have benefited from friendly and helpful officemates and neighbor of JGB 5.328 (Jeff Senison, Kai Zhang and Dr. Robert Folk). I am also grateful for the friendliness and helpfulness of the rest of the Jackson School of Geosciences.

# Abstract

## Evaluation of a land surface solar radiation partitioning scheme using remote sensing and site level FPAR datasets

Kai Wang, M.S. Geo.Sci.

The University of Texas at Austin, 2013

Supervisor: Robert E. Dickinson

Land surface covers only 30% of the global surface, but contributes largely to the intricacy of the climate system by exchanging water and energy with the overlying atmosphere. The partitioning of incident solar radiation among various components at the land surface, especially vegetation and underlying soil, determines the energy absorbed by vegetation, evapotranspiration, partitioning between surface sensible and latent heat fluxes, and the energy and water exchange between the land surface and the atmosphere. Because of its significance in climate model, land surface model solar radiation partitioning scheme should be evaluated in order to ensure its accuracy in reproducing these naturally complicated processes. However, few studies evaluated this part of climate model. This study examines a land surface solar radiation partitioning scheme, i.e., that of the Community Land Model version 4 (CLM4) with coupled carbon and nitrogen cycles.

Taking advantage of multiple remote sensing fraction of absorbed photosynthetically active radiation (FPAR) datasets, ground observations and a unique 28-year FPAR dataset derived from the Global Inventory Modeling and Mapping Studies (GIMMS) Normalized Difference Vegetation Index (NDVI) dataset,

we evaluated the CLM4 FPAR's seasonal cycle, diurnal cycle, long-term trends and spatial patterns. Our findings show the model roughly agrees with observations in the seasonal cycle , long-tern trend and spatial patterns but does not reproduce the diurnal cycle. Discrepancies also exist in seasonality magnitudes, peak value months and spatial heterogeneity. We identified the discrepancy in the diurnal cycle as due to the absence of dependence on sun angle in the model. Implementation of sun angle dependence in a one-dimensional (1-D) model is proposed. The need for better relating vegetation to climate in the model indicated by long-term trends is also noted. Evaluation of the CLM4 land surface solar radiation partitioning scheme using remote sensing and site level FPAR datasets provides targets for future development in its representation of this naturally complicated process.

# Table of Contents

# List of Figures

# List of Tables

# Chapter 1: Introduction

The partitioning of incident solar radiation among various components at the land surface, especially vegetation and underlying soil, determines the energy absorbed by vegetation, evapotranspiration, partitioning between surface sensible and latent heat fluxes, and the energy and water exchange between the land surface and the atmosphere [1–7]. How solar radiation reaches underlying soil through between-crown gaps and within-crown gaps is an essential part of micrometeorological, climatological, biogeochemical and hydrological modeling [8–12].

Various authors have explored numerical solutions to the partitioning problem, in both one-Dimensional (1-D) and three-Dimensional (3-D) geometries [10,13–16]. Though the complexity of the problem fully justifies the need for a 3-D model, 1-D models have been able to approximate it in a relatively simple form, give reasonable results and thus have been popular [13,14].

In the Community Land Model (version 4.0, CLM4), this process is formulated by a 1-D land surface solar radiation partitioning scheme: each sub-grid land cover type, plant functional type (PFT) patch and bare soil, is a separate column for energy calculation [15,17]; a 1-D radiative transfer approximation is employed to simulate the radiative transfer process within canopy at PFT level [15].

The fraction of absorbed photosynthetically active radiation (FPAR) is regarded as a diagnostic parameter for solar radiation partitioning scheme. FPAR is defined to be the fraction of PAR absorbed by the canopy [30], and hence, should be mainly decided by the radiative transfer process within the canopy. However, it can also be affected by the solar radiation reflected by the ground since plants are not separated from their background in FPAR observations, either at site level or in remote sensing. Below-canopy PAR sensors at flux sites measure not only the PAR

transmitted through the canopy but also the PAR directly incident on the ground; digital information at each pixel in remote sensing represents the averaged spectral information from each surface type within the instantaneous field of view (IFOV). Therefore FPAR is employed as the diagnostic parameter for the land surface solar radiation partitioning scheme.

Few studies evaluated the solar energy partitioning schemes in climate models with FPAR datasets, among which analysis mainly focused on differences in absolute value between model and observations. Tian et al. [18] compared seasonal and spatial variations of FPAR from MODIS and CLM2.0 from 2000 to 2002, and found that the CLM2.0 underestimated FPAR in the Southern Hemisphere and overestimated FPAR over most areas in the Northern Hemisphere. Senna et al. [19] compared FPAR from field measurements, MODIS and IBIS simulations, and showed that IBIS underestimated FPAR for the tropical forest. Yet, in terms of dynamics and spatial patterns, never has a climate model solar radiation partitioning scheme been comprehensively evaluated.

My work follows these previous works, but gives a comprehensive evaluation of CLM4 with dynamics of FPAR's seasonal cycle, diurnal cycle, long-term trends and spatial patterns. The seasonal cycle of FPAR is essentially driven by leaf presence, growth and foliage, so it can be interpreted as a manifestation of plant phenology. The diurnal FPAR cycle, however, is a more complicated process. It is orchestrated by the angular effect of direct solar radiation, fraction of direct radiation in total solar radiation and vegetation coverage in the forest. The study of the diurnal cycle of FPAR is a novel utilization of flux tower observations. Diurnal cycle observations represent all aspects of canopy-sun-surrounding relations while traditional studies using site level observations focus on the seasonal cycle and absolute value at one point in time [19–23]. The long-term trends of FPAR could be

impacted by two factors: plant phenology changes, such as leaf area index (LAI) and leaf out time, and plant distribution changes [24]. In addition to temporal dynamics, FPAR spatial patterns are also evaluated. Spatial patterns are decided mainly by plant types and geographical conditions [25]. As analyzed above, the accuracy of the solar radiation partitioning solutions depends on not only the performance of the land surface solar radiation partitioning scheme but also on the accuracy of input information on vegetation (e.g., LAI) and other conditions. Therefore, our evaluation needs to generally identify the reasons for discrepancies and focus on those problems related to the land surface solar radiation partitioning scheme.

Current remote sensing (RS) data and the application of photosynthetically active radiation (PAR) sensors in flux tower networks provide appropriate observations for evaluating the CLM4 land surface radiation partitioning scheme. Some satellite FPAR datasets have been produced based on various retrieval algorithms and radiative transfer assumptions [20,26,27] Although different from each other in absolute values, most remote sensing FPAR products are compatible with each other in seasonal cycle and spatial pattern [23,25,28]. The application of PAR sensors in a flux tower network enables evaluations of the FPAR diurnal cycle. PAR sensors provide highly accurate measurements of PAR, and have been put into service in many flux tower sites [19,29,30]. A systematic FPAR observation should consist of three parameters: incident PAR, reflected PAR and PAR transmitted through the canopy. Transmitted PAR should be measured by a group of PAR sensors because it is highly location-sensitive. Such an integrated observing system exists at limited sites [29]. Hence, it is of great potential to use both satellite-based and site-level observations to investigate CLM4 performance regarding FPAR dynamics and spatial patterns.

In Chapter 2, I examine the credibility of remote sensing data sets by inter-comparison. A sun angle dependency in FPAR illustrated by site level FPAR observations is presented in Chapter 3. Evaluation result and discussions are in Chapter 4 with conclusions drawn in Chapter 5.

# Chapter 2: Remote Sensing FPAR

In order to be considered as benchmark, remote sensing observations should be proved reliable prior to evaluating the model. Although studies of satellite FPAR products have recognized their credibility in seasonal variability at site and regional levels, a global-scale evaluation with multiple products has not been presented. High levels of agreement among these datasets are expected, because it would suggest that these datasets are similar and are potentially correct. The more agreement, the more likely it is that the datasets are correctly capturing the variable. Here we show that there are general agreement in seasonal cycles and spatial patterns among these four remote sensing datasets despite differences in their absolute values.

## 2.1 Introduction to Data Sets Adopted in This Research

### 2.1.1 MODIS FPAR

The Moderate Resolution Imaging Spectroradiometer (MODIS) FPAR algorithm is based on 3-D radiative transfer theory. Inverse Look-Up-Tables (LUTs) are generated for six major biomes defined by MODIS; model configurations for each biome differ from each other by fractional coverage, structural characteristics including canopy height, leaf type and soil color. Measured surface reflectances (atmospherically corrected bidirectional reflectances) at a maximum of 7 spectral bands are used for the inversion [26]. The FPAR data was produced from Terra MODIS data. The MODIS daily product is computed daily at 1 km resolution globally. The maximum FPAR value (across the eight days) is selected for the 8-day product [31]. Based on the 8-day product, Zhao [32] produced an improved product with cloud-contaminated pixels gap-filled.

### 2.1.2 GIMMS FPAR3g/LAI3g

GIMMS FPAR3g/LAI3g is computed based on improved versions of MODIS FPAR/LAI [33,34] and GIMMS NDVI3g generated from the Advanced Very High Resolution Radiometeters (AVHRR) using an artificial neural network. GIMMS NDVI3g and its long-term (June 1981-2011) global coverage at frequent intervals provide a unique opportunity to explore vegetation long-term dynamics [35]. It is therefore used as the sole dataset for long-term trend evaluation. However, the AVHRR data lacks correction for aerosol scattering and water vapor absorption [36] , resulting in possible atmospheric artifacts in the GIMMS data sets.

### 2.1.3 JRC FPAR

The Joint Research Center (JRC) generic FPAR algorithm has been used to develop FPAR products for both Sea-viewing Wide Field-of-view Sensor (SeaWiFS) and MEdium Resolution Imaging Spectrometer (MERIS) [27,37]. It is not biome-specific but defines FPAR as "green" instantaneous FPAR under direct illumination. Its input data are top of atmosphere (TOA) BRFs in blue, red and near-infrared bands. Blue band is used to remove the atmospheric effects [38]. For the monthly composite, median values which is the closest to the temporal average estimated over the compositing period is selected to generate the statistics [39].

### 2.1.4 Previous Evaluation Summary

Many validation studies of these FPAR datasets have been done at various scales. Most of these studies focused on regional scales because it is easier to obtain accurate reference data for a specific area, either ground measurements or high spatial resolution satellite data [11,22,23,40,41]. Fensholt et al [40] evaluated MODIS FPAR in semi-arid West Africa and Senegal using in situ measurements, and found that MODIS FPAR captures the seasonal dynamics well but has an overestimation by

8~20% in a semi-arid environment. Huemmrich et al [23] conducted time-series validation of MODIS FPAR in a Kalahari woodland near Mongu in western Zambia using ground measurement. The result demonstrates a good agreement in the woodland canopy phonology despite a significant bias in absolute value. Steinberg et al [22] validated MODIS FPAR product in boreal forests of Alaska, using field measurements and high spatial resolution FPAR product from IKONOS and Landsat ETM+. They found that the MODIS product adequately captured seasonal variability associated with vegetation phenology but tended to overestimate FPAR relative to both ground measurements and landsat-derived estimates of FPAR. At larger scales, previous studies usually use inter-comparison between different RS FPAR datasets to evaluate their performance[25,28]. Weiss et al [28] used MODIS FPAR to validate and compare with CYCLOPES FPAR and found they have generally consistent seasonality. McCallum et al [25] compared four global FPAR datasets over Northern Eurasia for the year 2000, including MODIS, SeaWiFS (CYCLOPES and GLOBCARBON are the other two). They focused on differences in absolute values among the datasets and attributes discrepancies to different retrieval methods, use of LAI and land cover, snow effects. A generally conclusion could be drawn from these studies is that the seasonal variation in FPAR has been well captured despite the difference in absolute value.

### 2.2 Inter-comparison Result

Figure 1 displays global monthly mean FPAR from January 2003 to December 2005. It shows MODIS agrees well with GIMMS3g and SeaWiFS agrees well with MERIS. As a matter of fact, GIMMS-FPAR3g is derived based on empirical nonlinear relationship between AVHRR-NDVI and MODIS FPAR so it should be similar to MODIS FPAR; SeaWiFS and MERIS both use JRC generic algorithm and thus should have similar FPAR estimation. We also see a significant gap between

these two dataset groups: MODIS and GIMMS3g FPAR are significantly higher than SeaWiFS and MERIS FPAR. Due to the presence of such a discrepancy, we are not able to use to satellite observations as benchmark to evaluate model simulations regarding FPAR absolute value.

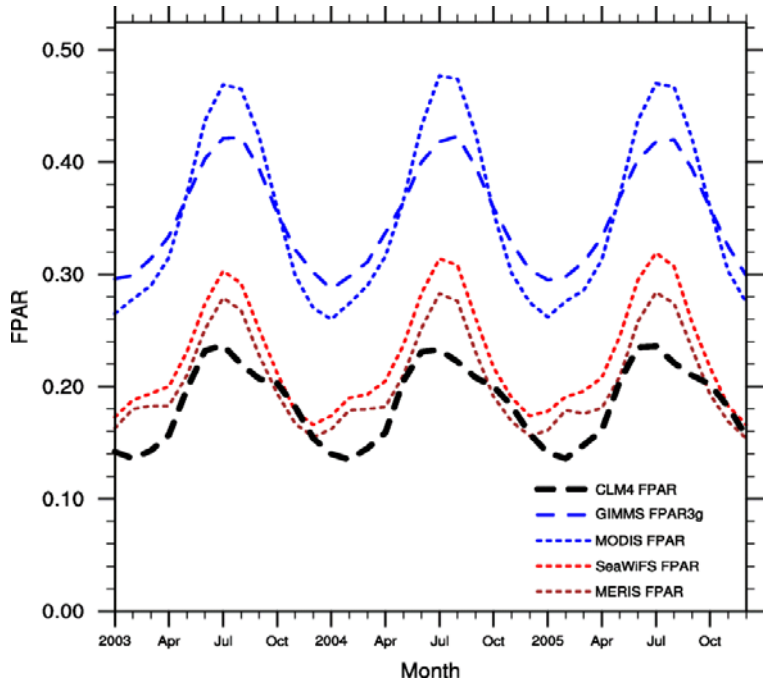


Figure 1:Comparison of monthly mean FPAR between remote sensing observations from 2003 to 2005.

Figure 2 shows global monthly mean anomalies, in which the difference in the absolute value has been removed by subtracting the temporal averaged value. It shows similar seasonal cycles among these four datasets, with maximum in July and minimum in December. The subtle difference is that MODIS and GIMMS3g FPAR have higher estimations from June to October and lower values from November to March than that of SeaWiFS and MERIS. These agreements among these four datasets in seasonality enable us to evaluate model FPAR seasonal cycle.

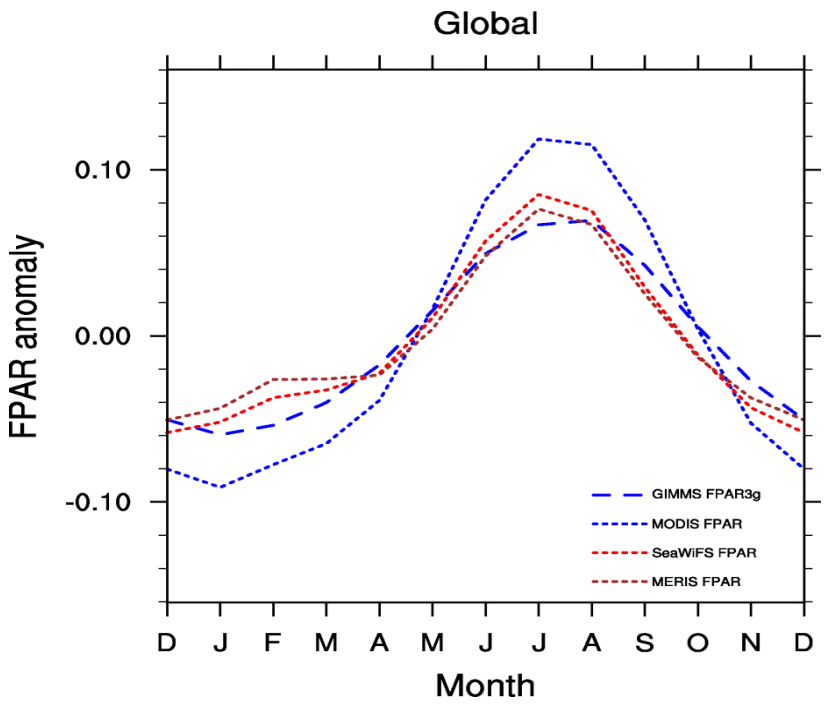


Figure 2: Comparison of average annual cycle of global monthly mean anomalies between remote sensing observations from 2003 to 2005.

Figure 3 displays zonal mean anomaly. It illustrated good agreement among four datasets but a subtle difference that MODIS and GIMSS3g FPAR are considerably higher in the tropical area. Figure 4a, 4b, 4c and 4d display the month of maximum FPAR from each datasets. They have good agreement in FPAR peaks month distribution. They peak in June, July and August in the northern hemisphere, while among December, January, February and March in the southern hemisphere. Such a pattern in FPAR peak month agree well with the month of maximum LAI from MODIS [42] . Therefore, these four datasets are reliable to evaluate the CLM4 FPAR spatial patterns.

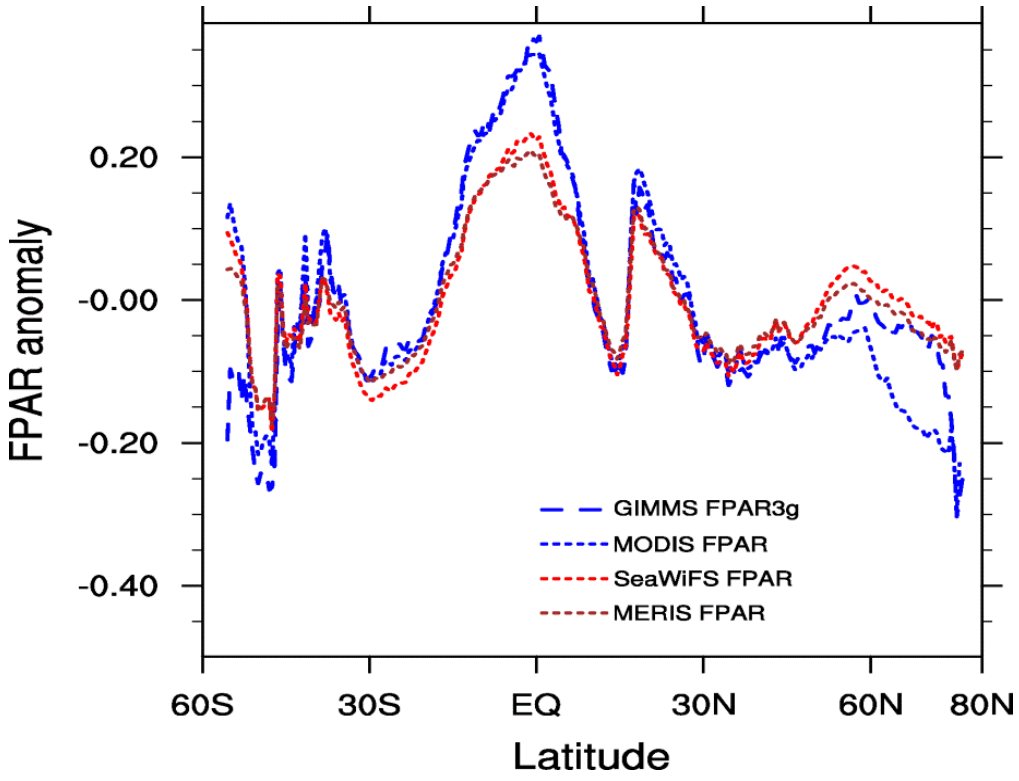


Figure 3: Comparison of zonal mean FPAR anomalies averaged between remote sensing observations from 2003 to 2005.

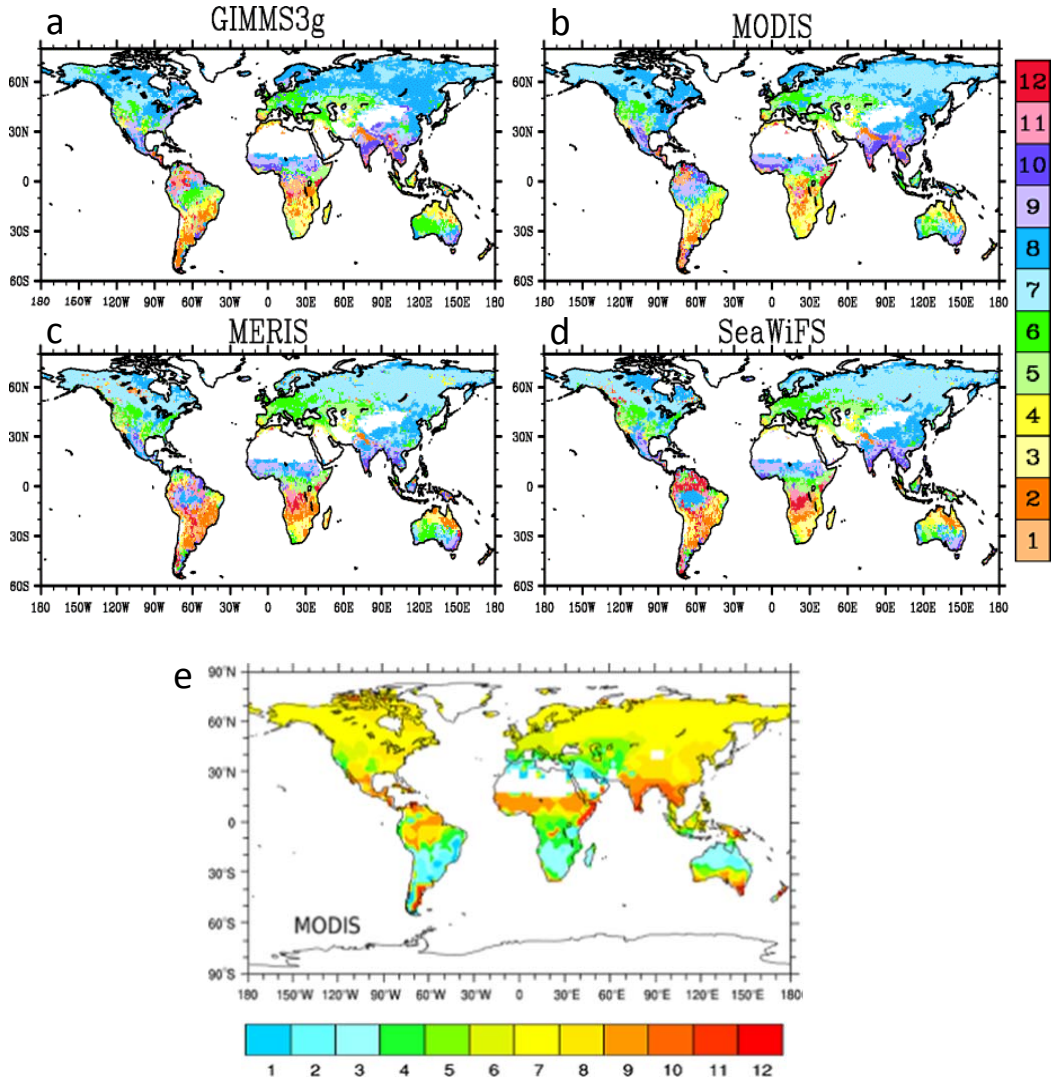


Figure 4: Month of maximum FPAR from: (a) GIMMS3g, (b) MODIS adjusted by Dr.Zhao, (c) MERIS, (d) SeaWiFS. (e) Month of maximum LAI from MODIS LAI adjusted also by Dr. Zhao's method cited from Ramderson's work (Randerson et al., 2009).

## 2.3 Conclusion and Summary

By comparing four datasets, we found high levels of agreements in seasonal and spatial variations among these remote sensing datasets, despite of the gaps among

them in terms of absolute value. Therefore, the model evaluation should focus mainly on seasonal and spatial variations and should avoid absolute value comparison.

# Chapter 3: Site level FPAR

In addition to remote sensing data, we also use site level FPAR data for diurnal evaluation. Previous studies primarily use site level data as a benchmark for absolute value. However, lacking remote sensing data agreement in absolute value, limited site level FPAR observations cannot support a global evaluation. Though site number is limited, observations are continuous and averaged every half-hour. We thus examined diurnal cycles and found a solar zenith angle dependency in FPAR.

## 3.1 Bartlett Experimental Forest

Bartlett Experimental Forest flux tower site (44.06 °N, 71.29 °W, and 272m elevation) is selected for site level evaluation in this study (Figure 5). It locates in north central New Hampshire, USA. The vegetation is primarily deciduous forest [29]. Plants are dominated by American beech (Fagus grandifolia), yellow birch (Betula alleghaniensis), sugar maple (Acer saccharum), red maple (Acer rubum), paper birch (Betula papyrifera), white ash (Fraxinus Americana), and pin cherry (Prunus pennsylvanica). Soils are moist but well drained spodosols. It is warm in summer and cold in winter. Winter season lasts from November to next May.

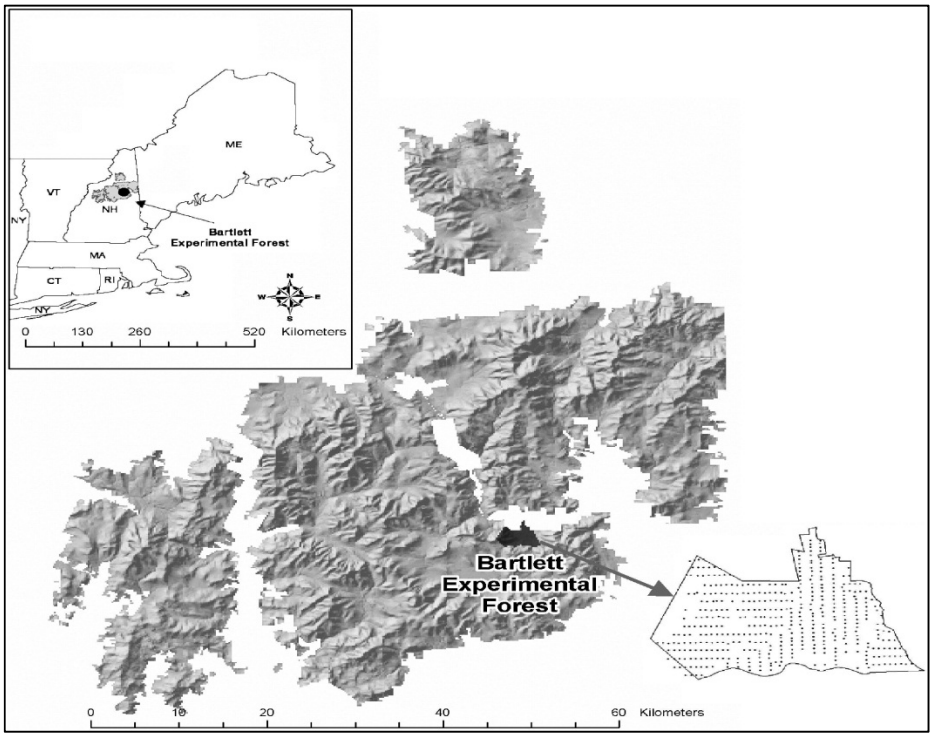


Figure 5: The map of the Bartlett Experimental Forest site copied from [Anderson et al., 2011].

### 3.2 Data Description

The flux tower is 25 m in height and set in a relatively flat area. Quantum sensors are placed above and below the vegetation canopy. Above-canopy sensors are located at the top of the tower, sensors facing upward measure the incident photosynthetic photon flux density ($Q_{incident}$) while sensors facing downward measure the photosynthetic photon flux density reflected from the canopy ($Q_{reflected}$). Six below-canopy sensors are placed in a circle (radius=15m) centered at the base of the tower [29]. They face upward and thereby measure the photon flux density transmitted through the canopies or gaps ($Q_{transmitted}$). Site-level FPAR is calculated by:

$$FPAR = \frac{Q_{incident} - Q_{reflected} - Q_{transmitted}}{Q_{incident}} \quad (1)$$

Observations of cloudy and rainy days are eliminated, because clouds and aerosols control the ratio of diffuse to total incident solar radiation [Wang et al., 2008] and diffuse radiation is not sensitive to the solar angle.

### 3.3 Diurnal Cycle

Figure 6 shows FPAR for each day in 2005 and 2006 from observations. It shows the minimum value occurring around noon in the early-growing months (March, April and May, MAM). The diunal cycle is that a canopy attenuates a larger fraction of the incident solar radiation in the morning and a much smaller share at noon. From morning to noon with one day, the canopy cannot change much so the main changing factor is the sun angle. FPAR thus is expected to have a sun angle dependency. We will explain this solar angular effect in FPAR this in next section.

Figure 7 shows the monthly GPP estimation from site observations. It shows that the vegetation at the site starts photosynthetic activities in March and peak in

July. This peak possibly indicates the fully-grown canopy (i.e., high LAI values). By comparing Figure 6 and Figure 7, we notice that the diurnal cycle is more significant before the GPP peak month (usually June for this site). One possible reason is that the between-crown gaps have been filled in by growth of leaves (high LAI) when GPP peaks. This assertion might explain the inter-annual differences between 2005 and 2006. Diurnal cycles exist with a clear valley pattern around noon after the GPP peak (July) in 2005 but not in 2006. Correspondingly, the GPP peak in 2005 is around 0.5 $\mu mol/(m^2 s)$ lower than that in 2006 (Figure 7). Since GPP is a good indicator for LAI, the lower GPP in 2005 suggests a lower LAI, and thus between-crown gaps cannot be filled by lower LAI canopies.

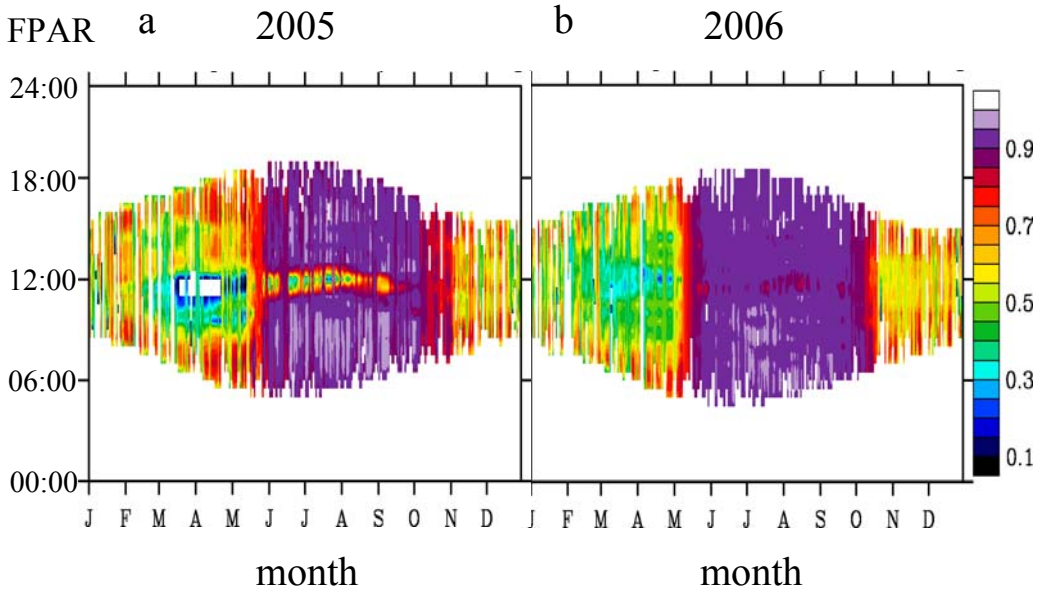


Figure 6: FPAR diurnal cycles of Bartlett Experimental Forest flux tower observation (a for 2005 and b for 2006). Cloudy and rainy days, observations with incident PAR lower than 50 μmol/(m^2 s) are removed in the site data.

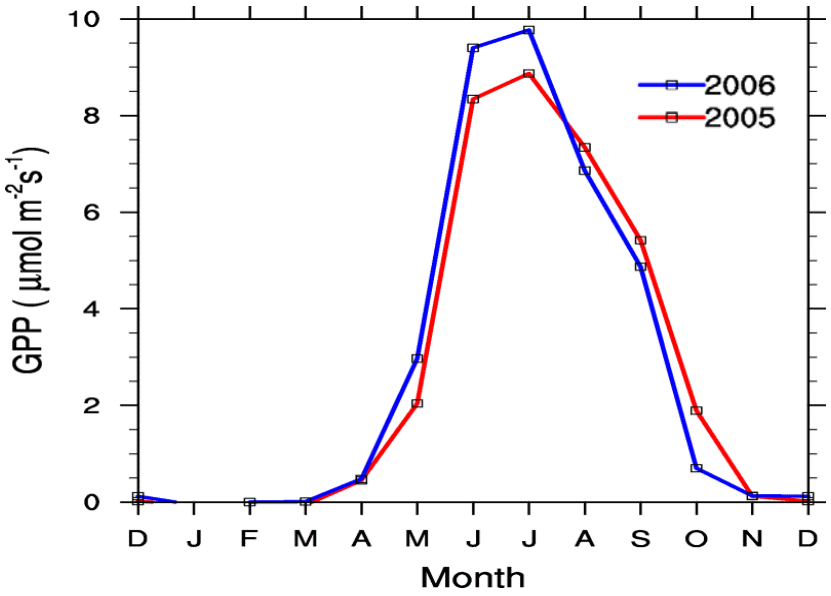


Figure 7: The annual cycle of monthly mean GPP from Bartlett Experimental Forest flux tower observations for the year 2005 and 2006.

### 3.4 Angular Effect in FPAR

To illustrate the angular effect in FPAR with direct solar radiation, we regard tree crowns as spheroids-on-sticks (Figure 8). $K_g$ and $K_c$ are the sunlit background portion and the sunlit canopy portion, respectively. They correspond to the areal fraction of ground and canopy under direct solar radiation.

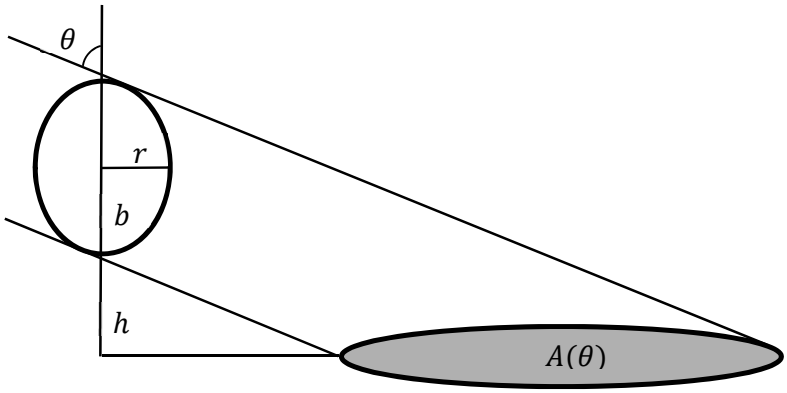


Figure 8: Geometry of a spheroid-on-a-stick, with three parameters: h, stem height from ground to the bottom of crown, and r and b, the horizontal and vertical radius of the spheroid, redrawn from [Strahler and Jupp, 1990].

According to the Boolean Scene Model introduced in [43], in a sparsely random distribution of the spheroids, the sunlit background portion is:

$$K_g = e^{-\lambda A_v(\theta)} \tag{2}$$

where $\lambda = \frac{\mathrm{n}}{\mathrm{A}}$ is the number of canopies in a unit of surface area, and $\mathrm{A}(\theta)$ is the average areal projection of the canopy onto the background at the zenith angle θ. From this expression for $\mathrm{K_g}$, the proportion of sunlit canopy portion can be immediately obtained, since both sum to 1.

$$K_c = 1 - e^{-\lambda A_v(\theta)} \tag{3}$$

For a single canopy area at vertical angle, $\mathrm{A_v}(0) = \pi \mathrm{rb}$, where r and b are the horizontal and vertical radius of the spheroid, respectively. For the off-vertical angle, $\mathrm{A_v}(\theta) = \pi \mathrm{rb}/\cos\theta$. Thus, we have:

$$K_c = 1 - e^{-\lambda A_v(\theta)/cos\theta} \tag{4}$$

Therefore, as the solar zenith angle decrease, the canopy intercepts less direct solar radiation, resulting in the angular effects in FPAR under direct solar radiation. It

is important to note that such an effect is restricted to sparse vegetation. For a fully-vegetated area, the angular effect is neglectable, because the bare soil is thoroughly covered by the vegetation and thus receives little solar radiation no matter how the solar zenith angle changes.

### 3.5 Absolute Value

Discrepancies among satellite-based FPAR products have been noted in many remote sensing evaluation papers [25,28,44]. Previous studies have identified several factors contributing to these discrepancies: First, radiative assumptions are different for different retrieval algorithms, though their influences require more study. Second, their statistical methods differ. MODIS selects the maximum FPAR (across the eight days) for the 8-day product [31] while SeaWiFS and MERIS use the median value in generating their products [39]. We propose another important reason for these discrepancies: the passing time is different for each satellite. We have illustrated how the angular effect in direct solar radiation leads to an FPAR difference. MODIS-Terra, SeaWiFS and MERIS satellite all have different passing time, as such their absolute values should differ from each other. Therefore, CLM4-FPAR's absolute value will not be evaluated in this study due to the absence of a benchmark. The difference in the absolute value is removed by subtracting the temporal averaged value for evaluation on seasonal and diurnal cycles and spatial patterns. The absolute value is used to calculate linear regression in long-term trend analysis, but does not affect the slope which is the key statistical parameter we analyzed.

### 3.6 Conclusion and Summary

In this chapter, we analyzed the Bartlett Experimental Forest flux tower observation and found a diurnal cycle characterized with the minimum value occurring around noon in the early-growing months. Such a diurnal cycle can be

explained by the dependence of the sun angle in FPAR. Furthermore, different remote sensing FPAR data should not agree in absolute value, because different satellite passing time would lead to different FPAR value. Hence, we will not evaluate model's performance based on its absolute value.

# Chapter 4: Evaluation of CLM4 FPAR

## 4.1 CLM4 FPAR Parameterization

There are two factors entering into the models calculation of FPAR, its prescription of LAI and its calculation of the radiation. These provide possible reasons for discrepancy: unrealistic LAI and unrealistic radiation partition scheme. In order to evaluate radiation partitioning scheme, we need to identify the reasons for FPAR discrepancies and then focus on those related to solar radiation partitioning scheme.

### 4.1.1 CLM4 FPAR

As the diagnostic parameter for the model, FPAR's accuracy reflects justifications of the land surface solar radiation scheme, but is not limited to this. Solar radiation (i.e., direct vs. diffuse radiation) and plant phenology (i.e., leaf area index (LAI)) are two factors also entering into the model's calculation of FPAR. In this study, solar radiation (including direct and diffuse radiation), as prescribed in forcing data CRUNCEP (available at http://dods.extra.cea.fr/data/p529viov/cruncep), as estimated based on meteorological station observations (CRU dataset) and reanalysis product (NCEP dataset).

CLM4 represents the land surface as a hierarchy of subgrid types including glacier, lake, wetland, urban, and vegetated landunits. The vegetated part is further divided into patches of 16 PFTs and bare soil. Each subgrid land cover type is a separate column for energy and water calculation [15].

In each PFT patch, the vegetation fractional coverage is 100%. The two-stream module is employed to calculate the solar radiant fluxes that are reflected, transmitted, absorbed by the canopy, and that are absorbed by the underlying soil. Several assumptions are made, including that fluxes are isotropic in only two directions (upward and downward), the canopy is horizontally homogenous and elements inside the canopy (including leaves, stems, and trunks) are randomly

distributed. The daily output of CLM4 sums up the fluxes from each PFT that includes bare soil and accounts for the fraction of vegetated area in the grid. In this study, CLM4 FPAR is defined as:

$$FPAR = \frac{\sum_{i=1}^{16} w_i I_{b,i} + \sum_{i=1}^{16} w_i I_{d,i}}{\sum_{i=0}^{16} w_i S_{b,i}^{\downarrow} + \sum_{i=0}^{16} w_i S_{d,i}^{\downarrow}} \quad (5)$$

where $I_{b,i}(I_{d,i})$ is the direct (diffuse) solar radiation absorbed by the canopy in the visible band for plant type i. $S_{b,i}^{\downarrow}(S_{d,i}^{\downarrow})$ is the direct (diffuse) incident solar radiation at the land part of the grid in the visual band for plant type i [18], and $w_i$ is the areal weighting of the plant functional type in the grid, $\sum_{i=0}^{16} w_i = 1$, including bare soil ($i = 0$).

As for plant phenology, the plant phenology cycle in the CLM4 is fully-prognostic, resulting from coupling Carbon-Nitrogen (CN) model: the seasonal timing of new vegetation growth and litterfall responds to soil and air temperature, soil water availability, and day-length, in varying degrees depending on a specified phenology type for each PFT. LAI calculation is based mainly on the specific leaf area SLA ($m^2$ one-sided leaf area per gC) and the total canopy leaf carbon ($C_L$, $gC \cdot m^{-2}$ ground area) [45]. A linear relationship between SLA and canopy depth is assumed as:

$$SLA(X) = SLA_0 + mx \quad (6)$$

where $SLA_0$ is SLA at the top of the canopy, m is a linear coefficient, and x is a parameter describing the canopy depth as an overlying leaf area index. $SLA_0$ and m are both fixed for each PFT. Total canopy leaf carbon $C_L$ can be found by integrating over the canopy:

$$C_L = \int_0^L \frac{1}{SLA(x)} dx = \frac{ln[(mL+SLA_0)] - ln(SLA_0)}{m} \quad (7)$$

Given $C_L$ calculated from the CLM4, L can be solved as:

$$L = \frac{SLA_0[exp(mC_L)-1]}{m} \quad (8)$$

$C_L$ is a dynamic carbon pool affected by gains from photosynthesis, and losses to litterfall and mortality, including from fire [46,47]. In addition to the dynamics of leaf carbon pool, feedbacks between carbon cycle and nitrogen cycle are also considered, which would also limit the rate of carbon accumulation in canopy leaf carbon [15].

### 4.1.2 Simulation Design

In this study the coupled Carbon-Nitrogen (CN) version of CLM4 was driven by historical meteorological data CRUNCEP (http://dods.extra.cea.fr/data/p529viov/cruncep/), land use and land cover, atmospheric $CO_2$ concentration, and anthropogenic nitrogen deposition. Beginning with the steady model state in 1901, CLM4 was run to 2009 with the previously mentioned historical forcings. Detailed information about the driver datasets and model settings can be referred to [48,49]. The half-degree monthly FPAR output during 2003-2005 was selected for direct comparison with all satellite observations due to the availability of remote sensing datasets. The period 1982-2009 was selected for inter-annual change trend comparison between CLM4 FPAR and GIMMS FPAR3g.

## 4.2 Assessment of Consistency between Model and Observation Data Sets

Several analyses were performed over various temporal and geographical extents. Diurnal cycle was performed over the Bartlett Experimental Forest flux tower site from 2005 to 2006, seasonal cycle and spatial patterns were performed globally from 2003 to 2005, and long-term trends were conducted globally over the 28-year period of 1982–2009.

Prior to the analysis, data were resampled by averaging at 0.5° resolution if needed, grids defined as non-vegetated in MODIS, and dominant vegetation distribution was masked in all datasets. To assess the consistency between the model simulated FPAR and observations, several sets of analyses were performed as follows:

### 4.2.1 Diurnal Cycle

Prior to the analysis, observation on rainy and cloudy days were eliminated, because clouds and aerosols control the ratio of diffuse to total incident solar radiation [50], and diffuse radiation is less sensitive to the solar angle. Rain and cloud are decided by precipitation measurement and diffuse solar radiation (if diffuse PAR > 500 μmol/(m2·s), respectively. To better present the diurnal cycle, half-hourly FPAR data were normalized at a daily level by:

$$FPAR_{n(i,j)} = \frac{FPAR_{a(i,j)}}{FPAR_{max(i)}} \quad (9)$$

where $FPAR_{n(i,j)}$ is normalized FPAR on day i, at time j, $FPAR_{a(i,j)}$ is FPAR on day i, at time j, $FPAR_{max(i)}$ is maximum FPAR on day i.

### 4.2.2 Seasonal Cycle

FPAR seasonal cycle comparisons are made at two spatial scales: global and aggregated by dominant MODIS vegetation types. The MODIS FPAR algorithm uses the MODIS land cover product with the International Geosphere Biosphere Program (IGBP) classes [44,51]. The JRC generic FPAR algorithm does not consider land cover type [45,46]. The CLM4 has a subgrid system representing vegetation as patches of PFTs that are derived from various datasets including MODIS Vegetation Continuous Fields data, AVHRR Continuous Fields Tree Cover Project data, MODIS global land cover mapping, Ramankutty and Foley global cropping, and Willmott and

Matsuura climate data set [52]. As MODIS and CLM4 use different vegetation classification systems, the dominant vegetation distribution from MODIS is employed for the comparison of this paper. We define the dominant biome type in each half-degree grid as the land cover for the grid [53]. Prior to the analysis, monthly FPAR were averaged for each grid over 2003 to 2005. Monthly FPAR data at global and biome levels were calculated by:

$$FPAR_{a(m,b)} = \frac{\sum_{i,j} FPAR_{a(m,i,j)} \times Area_{i,j} \times frac_{i,j,b}}{\sum_{i,j} Area_{i,j} \times frac_{i,j,b}} \quad (10)$$

where $FPAR_{a(m,b)}$ is FPAR in month m for biome b (or for the global, if $b = 0$), $FPAR_{a(m,i,j)}$ is FPAR at computational grid $(i, j)$ in month m, $Area_{i,j}$ is the area for the grid $(i, j)$, $frac_{i,j,b}$ is the fraction of land unit at computational grid $(i, j)$. Grids that are not dominated by the target biome were defined as $frac_{i,j,b} = 0$. Correlation coefficients (i.e., correlation and p-value) are calculated based on $FPAR_{a(m,b)}$. Monthly FPAR anomalies at global or biome levels were calculated by:

$$FPAR_{ano(m,b)} = FPAR_{a(m,b)} - FPAR_{mean(b)} \quad (11)$$

where $FPAR_{ano(m,b)}$ is FPAR anomaly in month m for biome b (or for the global, if $b = 0$), $FPAR_{mean(i)}$ is averaged FPAR over the whole time period.

### 4.2.3 Long-Term Trends

Long-term trends are calculated based on GIMMS FPAR3g and CLM4 FPAR from 1982 to 2009 by linear regression. For each 0.5° pixel, the slope and significance level (indicated by p-level) were calculated from time series comprised of 28 annual mean values (one value for each year from 1982 to 2009). Trends in LAI are also calculated in order to diagnose source discrepancies. ,

### 4.2.4 Zonal Patterns

Similar to monthly FPAR, zonal FPAR were also calculated by the grid area and land unit fraction:

$$FPAR_{a(i)} = \frac{\sum_j FPAR_{a(ij)} \times Area_{i,j} \times frac_{i,j}}{\sum_j Area_{i,j} \times frac_{i,j}} \quad (12)$$

where $FPAR_{a(i)}$ is the averaged FPAR for latitude band i. $FPAR_{a(i,j)}$ is FPAR at computational grid (i, j), $Area_{i,j}$ is the area for the grid (i, j), $frac_{i,j}$ is the fraction of land unit at computational grid (i, j). Zonal FPAR anomalies at global or biome level were calculated by:

$$FPAR_{ano(i)} = FPAR_{a(i)} - FPAR_{mean(i)} \quad (13)$$

where $FPAR_{ano(i)}$ is FPAR anomaly for computational latitude band i, $FPAR_{mean(lat)}$ is the mean value for the averaged FPAR of all latitude bands.

## 4.3 Evaluation Results Evaluation Results

### 4.3.1 Dominant PFT Distribution

In this study, FPAR comparisons are made at two spatial scales: global and aggregated by dominant PFT. The MODIS FPAR algorithm uses the MODIS land cover product with the International Geosphere Biosphere Programme (IGBP) classes [35]. The JRC generic FPAR algorithm does not consider land cover type [36,37]. The CLM4 has a subgrid system representing vegetation as patches of PFTs that are derived from various datasets including MODIS Vegetation Continuous Fields data, AVHRR Continuous Fields Tree Cover Project data, MODIS global land cover mapping, Ramankutty and Foley global cropping and Willmott and Matsuura climate data set [50]. Since MODIS and CLM4 use different vegetation classification systems, the dominant PFT distribution from MODIS is employed for the comparison of this

paper. We define the dominant biome type in each half-degree grid as the land cover for the grid [51].

### 4.3.2 Seasonal Cycle

To evaluate differences in FPAR seasonality independent of the discrepancies in FPAR absolute values, we calculated the anomalies of the global mean FPAR from CLM4 FPAR and satellite-based FPAR from 2003 to 2005 (Figure 9a). CLM4 generally captured the seasonal variations displayed by satellite-based FPAR. However, the peak in CLM4 FPAR is about 1-2 months earlier than that of the remote sensing observations and the seasonal variations in CLM4 FPAR are smaller than in the RS observations.

In addition to global level, we selected ten major PFTs among the seventeen PFTs defined by the IGBP to conduct the comparison. Figure 9b-k shows CLM4 generally captured the seasonal variations displayed by satellite-based FPAR. CLM4-FPAR and remote sensing FPAR have good correlation over the global and most PFTs (Table 1). However, CLM4 FPAR generally has a smaller seasonality and a shift in peak months. For savannas, CLM4 fails to capture the peak and trough months, and seasonality in CLM4 is less pronounced than in the satellite observations (Figure 9i). Savannas-dominated grids exist in the Sahel region, southeast Africa and in the western part of South America. These areas are characterized by seasonal water availability, with most of their rainfall confined to one season. Correspondingly, we can see strong seasonality from the satellite observations (Figure 9i). However, such a discrepancy in seasonality is possibly related to the model parameterization of LAI estimation rather than the land surface solar radiation partitioning scheme. It should be noted that the model and remote sensing agree well in that evergreen broadleaf forest retains a rather stable FPAR all year round, though the correlation between

them is rather low due to discrepancies in anomalies. However, their anomalies vary through a range smaller than 0.05 (Figure 9c), which is consistent with the relatively stable phenology in tropical rainforest.

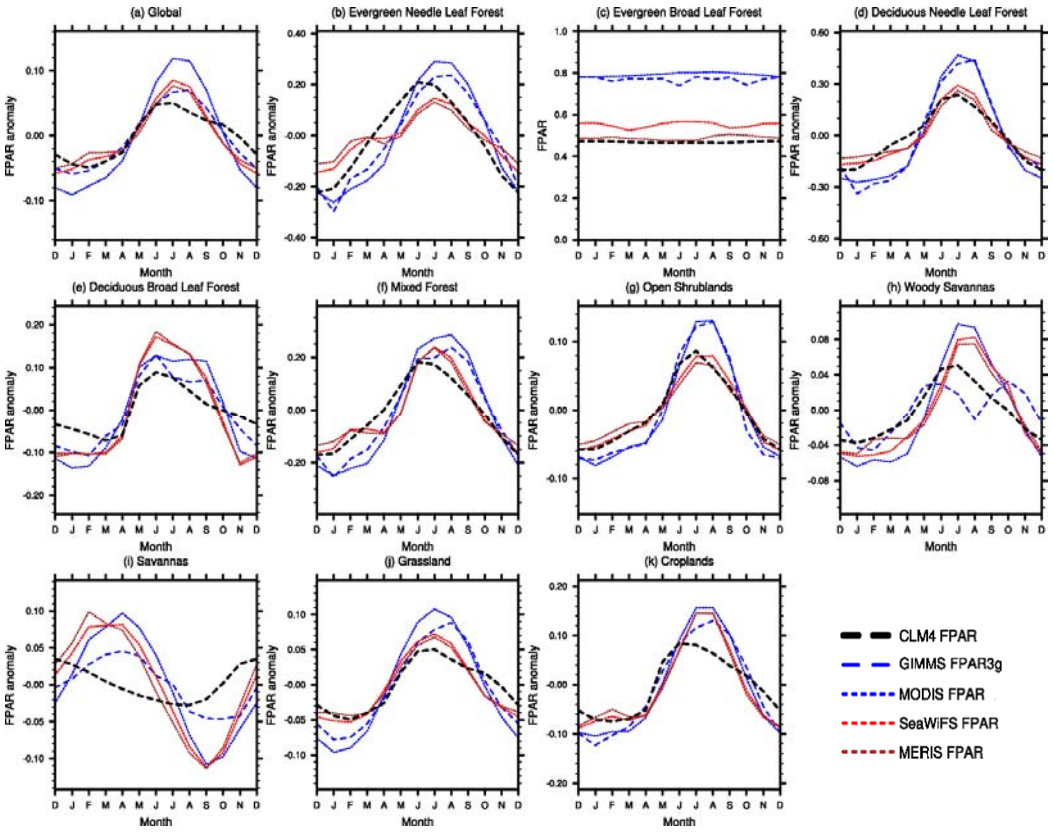


Figure 9: Comparison of 2003 to 2005 average seasonal cycle between remotely sensed FPAR and CLM4 FPAR at global level and PFT level: (a) global level, (b) evergreen needleleaf forest, (c) Evergreen broadleaf forest is compared based on FPAR absolute value due to its special seasonality, (d) deciduous needleleaf forest, (e) deciduous broadleaf forest, (f) mixed forests, (g) open shrublands, (h) woody savannas, (i) grassland, (j) croplands, (k) savannas.

| | GIMMS3g | | MODIS | | SeaWiFS | | MERIS | |
|---|---|---|---|---|---|---|---|---|
| | $\gamma$ | p-value | $\gamma$ | p-value | $\gamma$ | p-value | $\gamma$ | p-value |
| Global | 0.953 | 3.36E-04 | 0.942 | 3.34E-04 | 0.894 | 8.65E-06 | 0.873 | 9.25E-05 |
| Evergreen Needle Leaf Forest | 0.86 | 0.66 | 0.86 | 3.28E-04 | 0.934 | 0.96 | 0.893 | 0.44 |
| Evergreen Broad Leaf Forest | 0.14 | 2.35E-05 | −0.860 | 4.10E-06 | −0.016 | 4.11E-07 | 0.246 | 5.25E-06 |
| Deciduous Needle Leaf Forest | 0.919 | 1.90E-05 | 0.944 | 1.91E-04 | 0.965 | 1.57E-05 | 0.941 | 6.61E-06 |
| Deciduous Broad Leaf Forest | 0.923 | 1.78E-05 | 0.875 | 2.92E-05 | 0.926 | 2.09E-05 | 0.938 | 4.34E-05 |
| Mixed Forest | 0.924 | 1.92E-07 | 0.916 | 4.78E-07 | 0.921 | 1.35E-08 | 0.908 | 1.01E-08 |
| Open Shrublands | 0.97 | 1.96E-02 | 0.964 | 2.56E-05 | 0.982 | 1.22E-04 | 0.983 | 2.55E-04 |
| Woody Savannas | 0.66 | 0.94 | 0.918 | 0.90 | 0.887 | 0.28 | 0.868 | 0.11 |
| Savannas | 0.024 | 1.80E-06 | 0.042 | 1.51E-06 | 0.341 | 1.35E-05 | 0.487 | 1.58E-05 |
| Grassland | 0.952 | 2.07E-06 | 0.954 | 1.13E-05 | 0.928 | 8.99E-05 | 0.926 | 2.43E-04 |
| Croplands | 0.953 | 1.70E-06 | 0.942 | 4.59E-06 | 0.894 | 8.83E-05 | 0.873 | 2.12E-04 |

Table 1: Correlation coefficient γ with P-value between CLM4-FPAR and satellite-observed FPAR annual cycle from 2003 to 2005.

In order to identify the reasons for the discrepancies in FPAR seasonality, we compared the seasonality of CLM4 LAI and GIMMS LAI3g to various estimates of FPAR (Figure 10). CLM4 LAI lacks seasonal variations in comparison with GIMMS LAI3g at the global level (Figure 10a.), which can explain why CLM4 FPAR has less seasonal variations. For savannas, significant disagreements in FPAR between model and observations are also shown to have similar discrepancies in LAI (Figure 10b). As asserted earlier, the FPAR seasonality could be considered as a manifestation of plant phenology. The comparisons between LAI and FPAR from the model and observations verify this assertion, and hence suggest that the discrepancies in seasonality between CLM4 FPAR and observations are due to problems in the calculation of LAI.

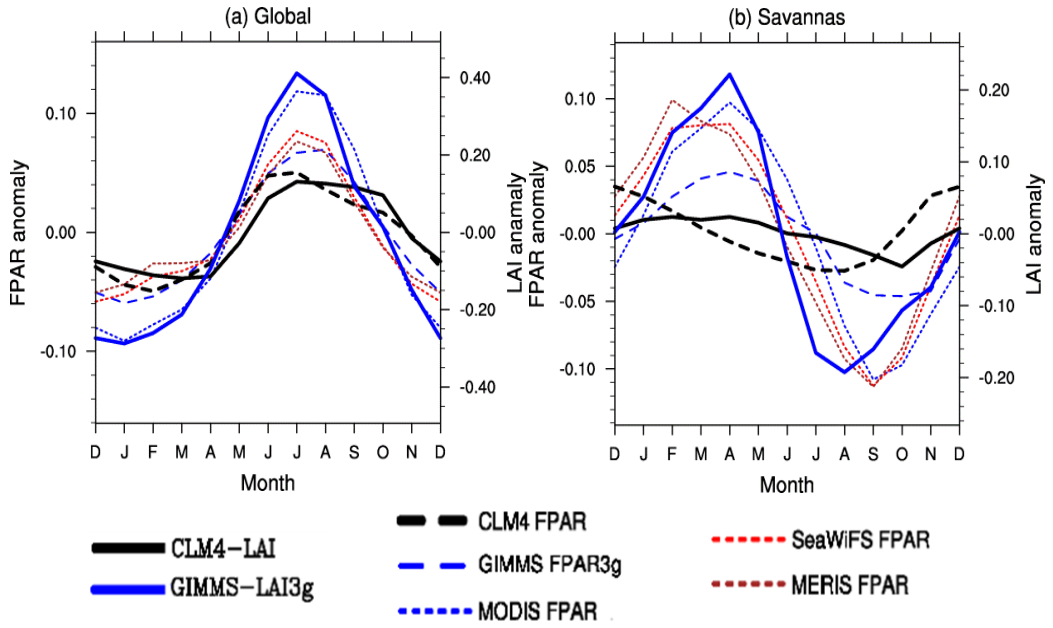


Figure 10: The annual cycle of monthly mean FPAR and LAI anomalies for (a) the global and (b) savannas (2003 ~ 2005).

### 4.3.3 Diurnal Cycle

As illustrated earlier regarding angular effect, a canopy attenuates a larger fraction of the incident solar radiation in the morning and a much smaller share at noon. Therefore FPAR is expected to have a valley around noon.

Figure 11 shows the normalized FPAR for each day in 2005 and 2006 from both observations and model. From the site-observed FPAR figures (Figure 11a and 11b), we can see the minimum value occurring around noon in the early-growing months (March, April and May, MAM), which is only around 30% of the maximum FPAR. It verifies the angular effects of FPAR that we illustrated earlier. Minimum value is also shown around noon in MAM in the model simulated FPAR (Figure 11c and 11d), but is around 80% of the maximum FPAR. Figure 7 shows the monthly GPP estimation from site observations. It shows that the vegetation at the site starts

photosynthetic activities in March and peak in July. This peak possibly indicates the fully-grown canopy (i.e., high LAI values). By comparing Figure 11 and Figure 7, we notice that the diurnal cycle is more significant before the GPP peak month (usually June for this site). One possible reason is that the between-crown gaps have been filled in by growth of leaves (high LAI) when GPP peaks. This assertion might explain the inter-annual differences between 2005 and 2006. Diurnal cycles exist with a clear valley pattern around noon after the GPP peak (July) in 2005 but not in 2006. Correspondingly, the GPP peak in 2005 is around 0.5 $\mu mol/(m^2 s)$ lower than that in 2006 (Figure 7). Since GPP is a good indicator for LAI, the lower GPP in 2005 suggests a lower LAI, and thus between-crown gaps cannot be filled by lower LAI canopies.

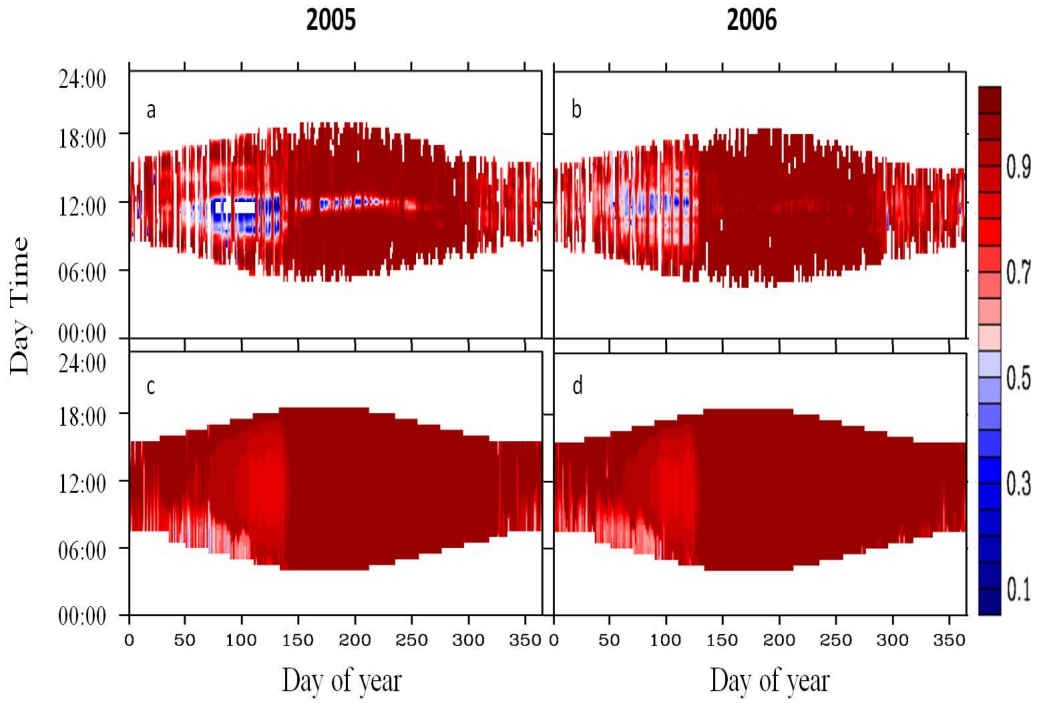


Figure 11: Comparisons of FPAR diurnal cycles between Bartlett Experimental Forest flux tower observation (a for 2005 and b for 2006) and CLM4 (c for 2005 and d for 2006). Cloudy and rainy days, observations with incident PAR lower than 50 $\mu mol/(m^2 s)$ are removed in the site data. For comparison, data sets are normalized to show the diurnal cycle.

### 4.3.4 Long-term Trends

Long-term trends are calculated based on GIMMS FPAR3g and CLM4 FPAR from 1982 to 2009 by linear regression. Trends in LAI are also calculated in order to diagnose source discrepancies. The availability of over 28 years of AVHRR NDVI observation offers a unique opportunity to evaluate the model's ability for simulating long-term change.

Figure 12 displays the statistics of the long-term analysis. The color represents the slope of linear regression and the black dots are grids exceeding 90% significance. GIMMS FPAR3g/LAI (Figure 12a and 12b) shows that Western Europe, Eastern America, the Sahel region, part of Eurasia and the northern high latitudes are the areas

with significant increasing trend in FPAR and LAI. Among these areas, changes in Western Europe are due to the afforestation of former arable land [52], an anthropogenic factor that is already included in the current CLM4. The rest of the areas are all transitional ecoregions: the Sahel region is a transition zone of semi-arid grasslands, savannas, steppes and thorn shrublands lying between the Sahara desert and the Sudanian Savannas [53]; Eastern America and part of Eurasia are both mostly covered by mixed forest consisting of coniferous and broadleaf trees; the northern high latitudes are mainly Arctic tundra ecosystem which are highly sensitive to temperature shifts [54]. As the satellite observations shows, these areas are highly sensitive to global climate change and thus have significant long-term trends.

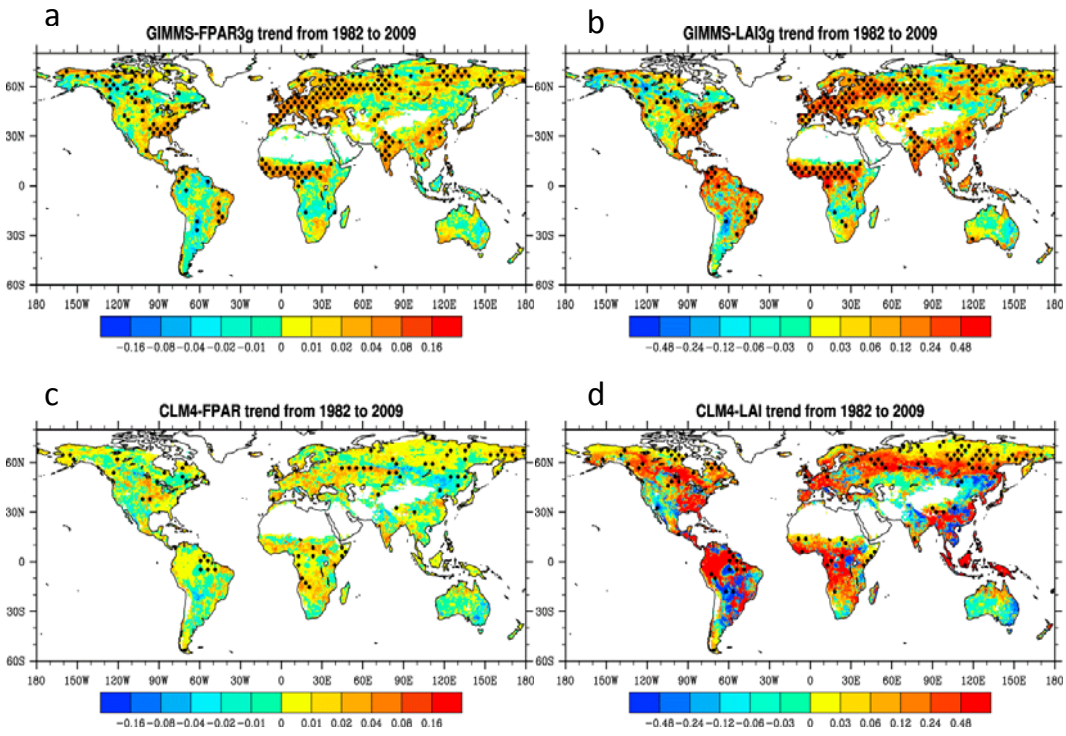


Figure 12: Global distribution of linear regression slopes in (a) GIMMS FPAR3g, (b) GIMMS LAI3g, (c) CLM4 FPAR and (d) CLM4 LAI from 1982 to 2009. Grids with slopes exceeding the 90% confidence level are marked with black dots

The CLM4 simulations are in broad agreements with the increasing trends illustrated by GIMMS3g datasets (Figure 12). However, the model has fewer grid cells exceeding statistical significance level of 90% (Figure 12). Since long-trends are primarily driven by changes in forcing factors (e.g., $CO_2$ concentration, precipitation and temperature), these discrepancies suggest that the CLM4 needs to improve its correlation between climate and vegetation. Annual changes of vegetation growth possibly caused by other factors such as nitrogen deposition and land use and land cover change are beyond the scope of this paper and are detailed in [49]. Although our study does not examine land cover change, extensive FPAR increase in the northern high latitudes suggests dynamic vegetation change (Figure 12b). As several studies asserted, shrub expansion exists in Northern Alaska, Siberia and the Pan-Arctic [55–57]. It would thus be necessary to employ a dynamic vegetation model (e.g., Dynamic Global Vegetation Model, DGVM) to reproduce expansions of certain plant types. In sum, we have two findings in regards to the CLM4: 1) CLM4 does capture the long trends in FPAR at the global level but has much smaller significance levels due to its excess variability in its annual values; 2) discrepancies in the northern high latitudes further suggest that CLM-DGVM is required to fully evaluate model's performance for long-term trends.

### 4.3.5 Spatial Pattern

The zonal anomalies of FPAR from 2003 to 2005 are displayed in Figure 13 and the correlation coefficients between CLM4 and RS FPAR are also calculated. CLM4 FPAR has a very similar pattern to that of remote sensing observations. Statistics shows they are highly correlated (0.879 for GIMMS3g, 0.997for MODIS and MERIS, and 0.990 for SeaWiFS), and these correlations are all significant ($p<5\%$). They all have peaks around the equator and 25°N, and troughs around 30°S

and 15°N. The difference between FPAR at the equator and the 25°N in CLM4 simulation is around 0.071, which is much smaller than that in GIMMS3g (0.203) and MODIS (0.162), and close to that in SeaWiFS (0.113) and MERIS (0.079).

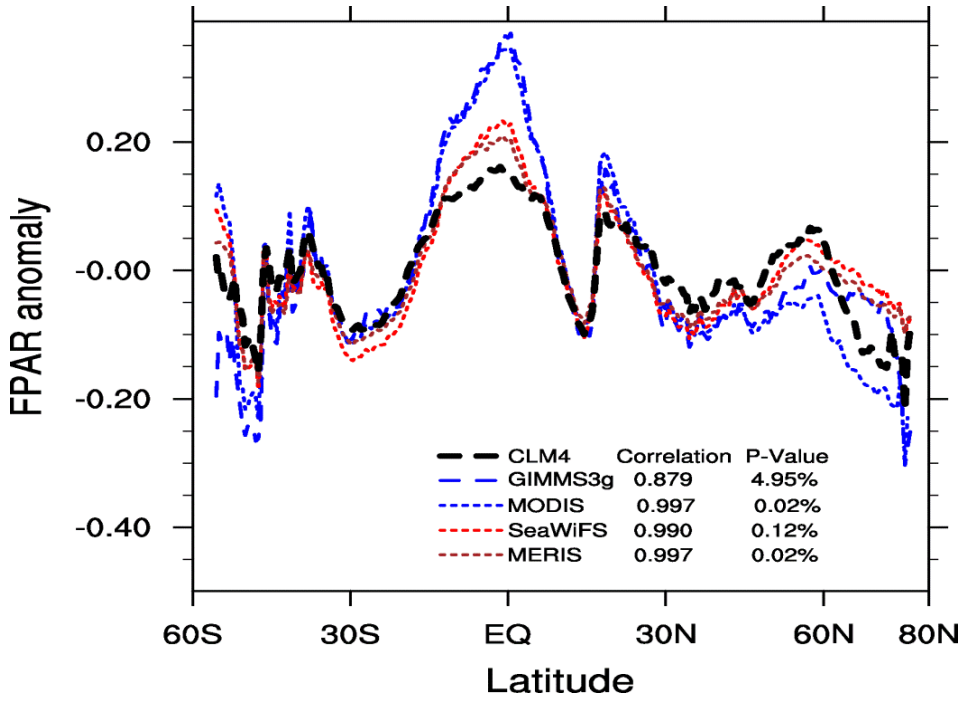


Figure 13: Comparison of zonal mean FPAR between RS observations and CLM4 FPAR averaged from 2003 to 2005. Correlation coefficients (i.e., correlation and p-value) are calculated between CLM4 zonal mean FPAR and each RS FPAR datasets

At the PFT level, the FPAR mean value from CLM4 simulation and remote sensing observations are compared in Figure 14. The CLM4 and remote sensing observations both have the highest value in broadleaf and savannas among all the PFTs, and also estimate the lowest FPARs in shrub-land and grassland.

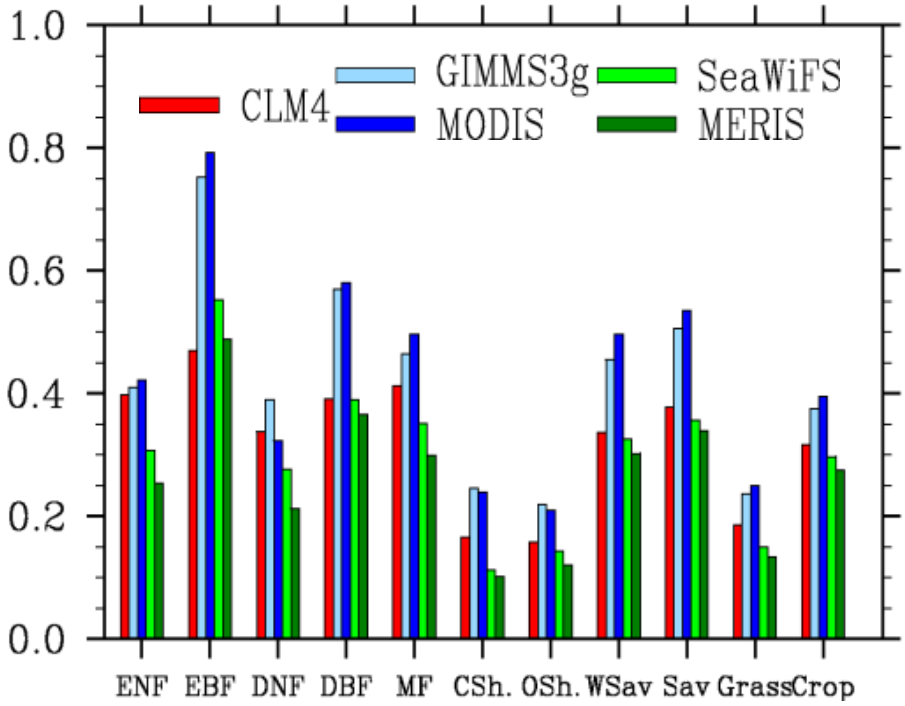


Figure 14: Comparison of FPAR at PFT level between RS observations and CLM4 FPAR averaged from 2003 to 2005

Figure 15 shows the month of maximum FPAR simulated by the CLM4. Compared with remote sensing observations (Figure 15a, 15b, 15c and 15d), the CLM4 does well in capturing the main characteristics of the FPAR peaking in JJA in the northern hemisphere and in DJFM in the southern hemisphere. However, the peak months in the CLM4 are generally one or two months earlier. The CLM4 simulations also have much less spatial heterogeneity in the month of maximum FPAR. Take north hemisphere for instance, satellite observations show FPAR peaks in June for Southern north America and west Europe, in July and August for northern north America and most Eurasia. The CLM4, however, estimates FPAR in most north hemisphere peaks in June with small high latitude area peaks in July.

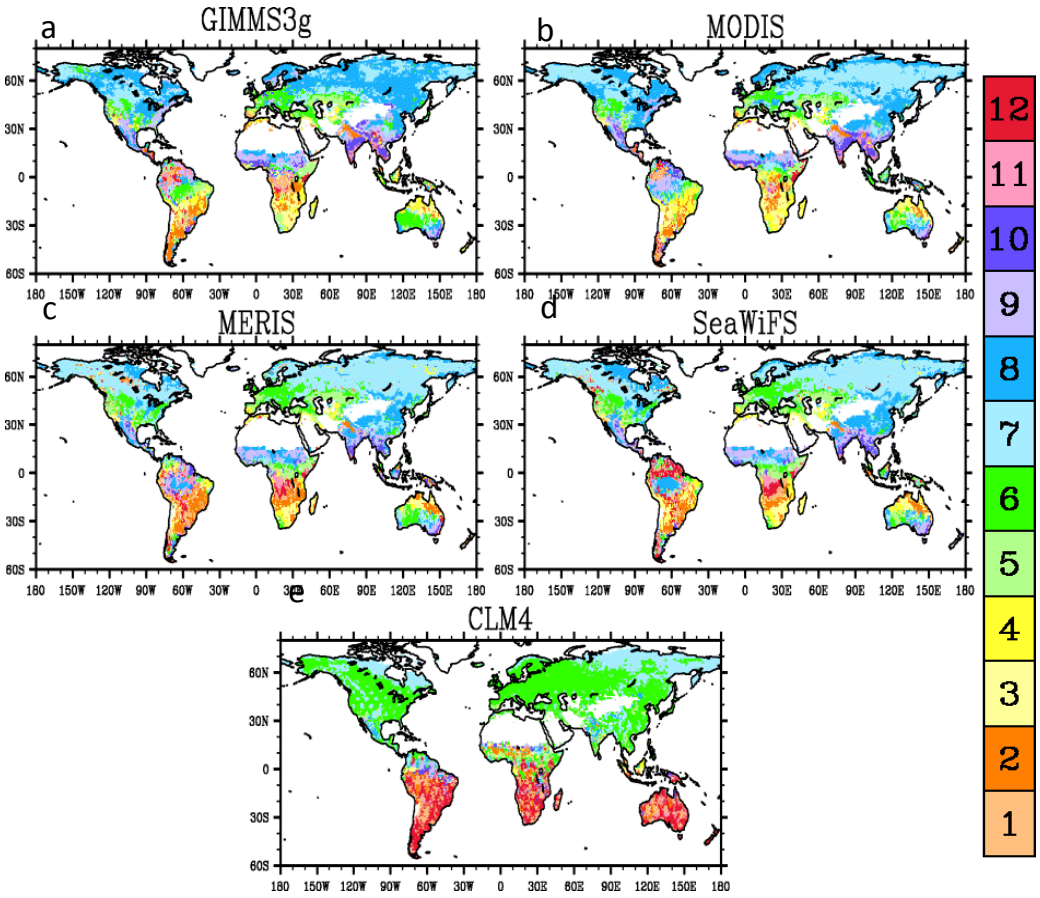


Figure 15: Comparison of month of maximum FPAR between RS observations and CLM4 FPAR averaged from 2003 to 2005, (a) GIMMS3g, (b) MODIS, (c) MERIS, (d) SeaWiFS, (e) CLM4 simulation

In the Amazon, CLM4 FPAR and satellite-based FPAR have an interesting discrepancy. The tropical forest FPAR has little seasonality as we can infer from its stable vegetation phenology, but the spatial distribution of month with the maximum FPAR value has an unexpected pattern. Divided by the equator, FPAR in the northern part of the Amazon peaks around November, December and January, while in the southern part it peaks around June, July, August and September (Figure 16a, 16b & 16d.). The probability density function of month with maximum FPAR value (Figure 16f and 16g.) verifies that such differences exist among satellite-based observations.

However, CLM4 FPAR has an opposite temporal-spatial distribution as we can see from Figure 16e. The probability density function of month with maximum FPAR value (Figure 16f and 16g) also verifies such differences between the CLM4 FPAR and satellite-based FPAR.

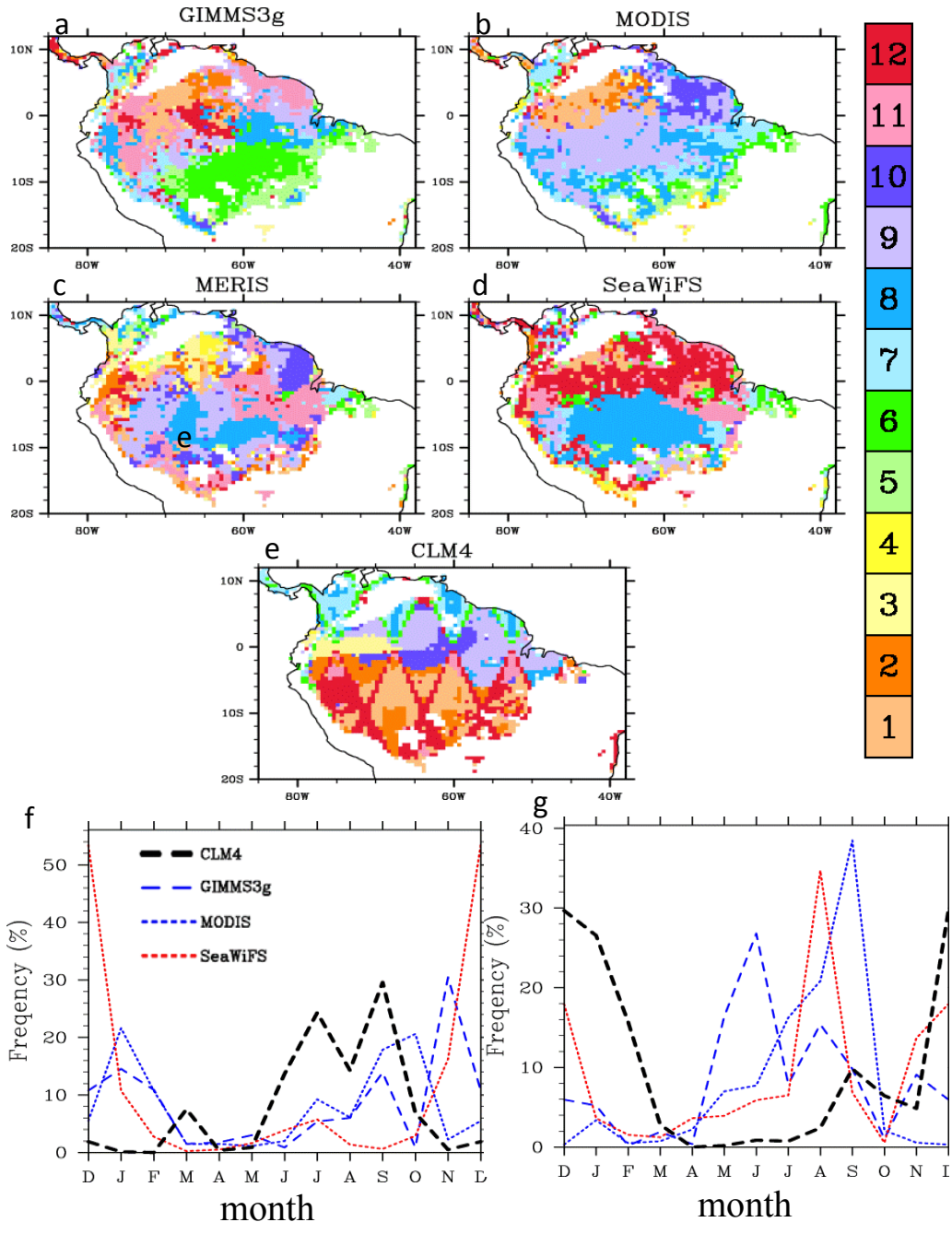


Figure 16: Month of maximum FPAR in the Amazon from (a) GIMMS3g, (b) MODIS, (c) MERIS, (d) SeaWiFS and (e) CLM4 simulation. Probability density function of maximum FPAR months in the northern (f) and southern (g) parts of the Amazon, divided by the equator.

### 4.4 Problems with the Diurnal Cycle in the CLM4

Comparison of site level observations and model simulations shows CLM4's FPAR has a slight diurnal cycle but at a much smaller magnitude than site level observation. Sun angle could influence radiation transfer process through both between-crown gap probability and within-crown gap probability [16]. In order to identify the reasons for the insignificant angular effect in the CLM4, we used the 2-stream module from the CLM4 and conducted a sensitivity test in a two-element model that is simplified from the current CLM4 land surface scheme. In the two-element model, a grid is set consisting of 2 patches: one is vegetated with 100% canopy coverage, its coverage is set to be fc; and the other is bare soil with a fraction of $(1 - \mathrm{fc})$. Related parameters are set as follows: 1) leaves and stems are set as blackbodies with reflectance and transmittance of 0; 2) ground albedo is 0.2 for both visual and infrared bands and for both direct and diffuse radiation; and 3) only direct solar radiation is considered. We calculate the fraction of canopy absorbed radiation in incident solar radiation for the whole grid under different fc and LAI conditions. A 3-D model is used for comparison because it takes into account the solar zenith angle, ground shadow, and overlaps between trees and radiatiave transfer processes within the canopy, and thus is regarded as a benchmark [10,58].

Experimental results (Figure 17) show the fraction of radiation absorbed by canopy would change according to the solar zenith angle when LAI is low (i.e., 0.5). This verifies that the insignificant diurnal cycle in the current CLM4 simulation is attributed to the 2-stream solution taking into account the angular effect inside the canopy layer. Such an angular effect in the canopy radiative transfer process only contributes to a small portion of the overall angular effect (as illustrated by the 3D scattering model in Figure 17) Therefore, the problem with the diurnal cycle in the

CLM4 is not the radiative transfer process within the canopy but rather the radiative transfer process outside of the canopy.

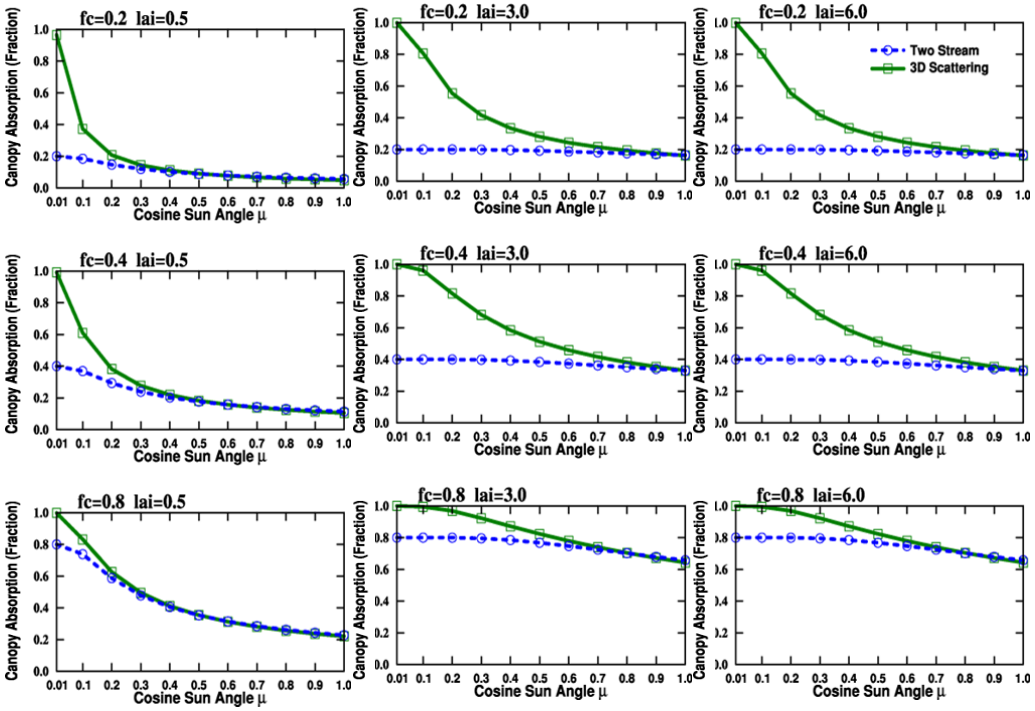


Figure 17: FPAR in relation to μ. Blue lines show simulations from the 2-stream solution in the CLM4 (blue) and green lines show simulation from the 3D scattering model at fc = 0.2, 0.4 and 0.8 and LAI= 0.5, 3.0 and 6.0.

Next we examine the current CLM4 patch framework. Bare soil and plants are separately allocated into different patches. For the patch with a plant type, the canopy fraction is set to be 100%. According to this assumption, the plants become "shadowless"; only the soil under the canopy might be blocked from solar radiation by the canopy, but the soil between canopies can always receive solar radiation without any canopy blocking as allocated in a separate patch. As a result of this "shadowless" canopy assumption, the bare soil is 100% exposed to solar radiation, and such a full-exposure in bare soil is the reason for the absences of an angular effect

in the current CLM4. Therefore, we need to introduce several parameters to present such an angular effect.

We propose a possible solution for this problem in the current CLM4 land surface scheme and illustrate it in a two-element model. The solution is based on the boundary condition inferred from the Boolean Scene Model: 1) vegetation has 100% coverage over the grid land when the solar zenith angle is $90^{\circ}$; and 2) a coverage of fc when the solar zenith angle is $0^{\circ}$, in the view of the sun.

By the view of direct solar radiation, the fraction of vegetation in the grid (fv) should be a function of fc and the solar zenith angle ($\theta$):

$$fv = e^{ln(fc)*\mu} \tag{14}$$

where $\mu = \cos\theta$. The fraction of bare soil in the sun's view should be $1 - e^{\ln(fc)*\mu}$, and the fraction of sunlit bare soil in total bare soil (fss) is:

$$fss = \frac{1-e^{ln(fc)*\mu}}{1-fc} \tag{15}$$

By this function, the bare soil would receive no direct solar radiation when $\mu = 0$ and would be 100% sunlit by direct solar radiation when $\mu = 1$.

This solution is a simplified approximation for the angular effect. Figure 18 shows it has good approximation when vegetation coverage is high or when LAI is high compared to the 2D scattering model. Larger discrepancies exist when both vegetation coverage and LAI are low. The relationship between vegetation coverage and LAI is not considered here but has been suggested by site level observations. As analyzed earlier, the inter-annual comparison of site level FPAR suggests that vegetation coverage (fc) changes according to LAI. Hence, LAI-fc relation should be taken into account to implement mathematical representation of an angular effect in the current CLM4 land surface solar radiation partitioning scheme.

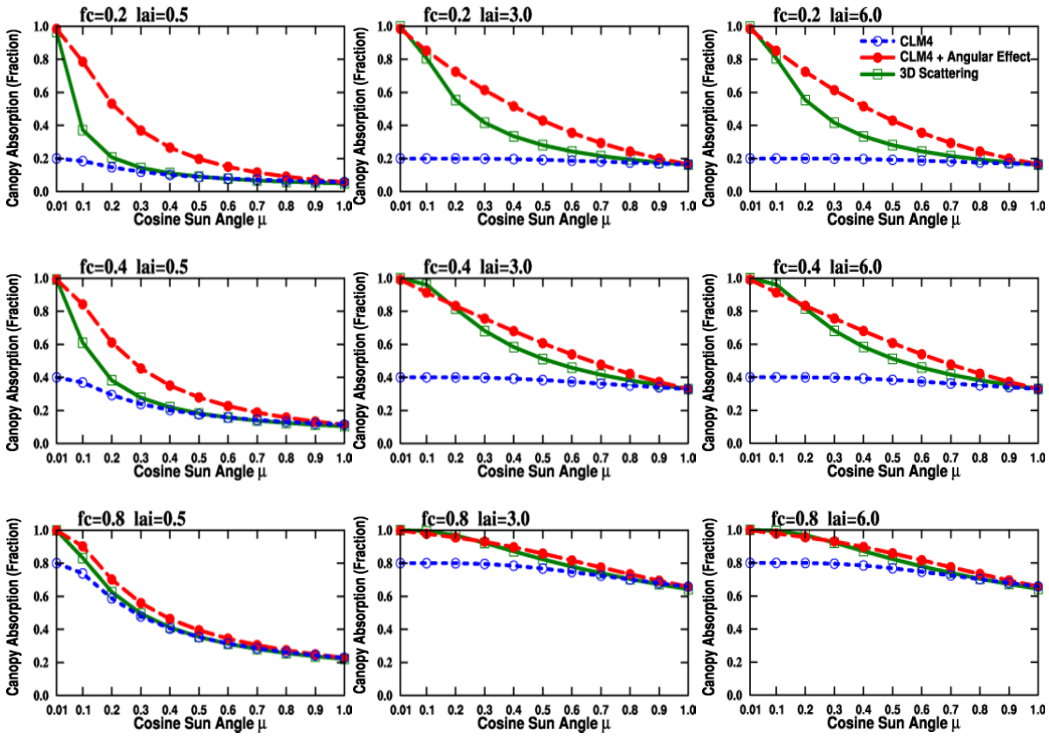


Figure 18: FPAR in relation to μ. Blue lines show simulations from the 2-stream solution in the CLM4 (blue), red lines show simulations from the proposed solution in the paper and green lines show simulations from the 3D scattering model at fc = 0.2, 0.4 and 0.8.

### 4.5 Spatial Patterns of Month with Maximum FPAR in the Amazon

As previously illustrated, both the northern and southern parts of the Amazon have different peak FPAR months opposite to their located hemispheres. The angular effect in FPAR is suspected to be one reason for this phenomenon. One major difference between the two regions is the solar zenith angle. According to the angular effect, FPAR would decrease as the solar zenith angle increases and the FPAR thus would not peak in local summer months. CLM4's opposite estimations then can be well explained because model does not consider the angular effect in FPAR. However, a weakness in this reasoning is that the angular effect is more significant for sparse vegetation but the Amazon rainforest is dense vegetation.

In addition to the angular effect, two other possibilities (i.e., cloud contamination and plant phenology) are also suspected to contribute to this phenomenon.

Cloud contamination is suspected to be a reason because remote sensing of the Amazon at visual bands has been complicated due to the presence of pertinacious cloud and aerosols during the rainy season. Remote sensing has made much effort in minimizing the cloud influence by: (1) recording cloud information into the raw data and pixels of good quality are selected for product generation; and (2) cloud-removal procedures to MODIS's surface reflectance products. However, these procedures still cannot totally avoid the potential systematical bias in FPAR. Since cloud contamination lowers the FPAR value, we would expect peak months to have the least precipitation in the region. For the southern part of the Amazon, FPAR peaks in June, July, August and September (Figure 16g) which are the months with much less rainfall (Figure 19). For the northern region, FPAR peaks in November, December and January (Figure 16f) by different satellite observations, which are months with

less rainfall in the region (Figure 19). Therefore, cloud contamination might be the reason for spatial patterns in satellite observations.

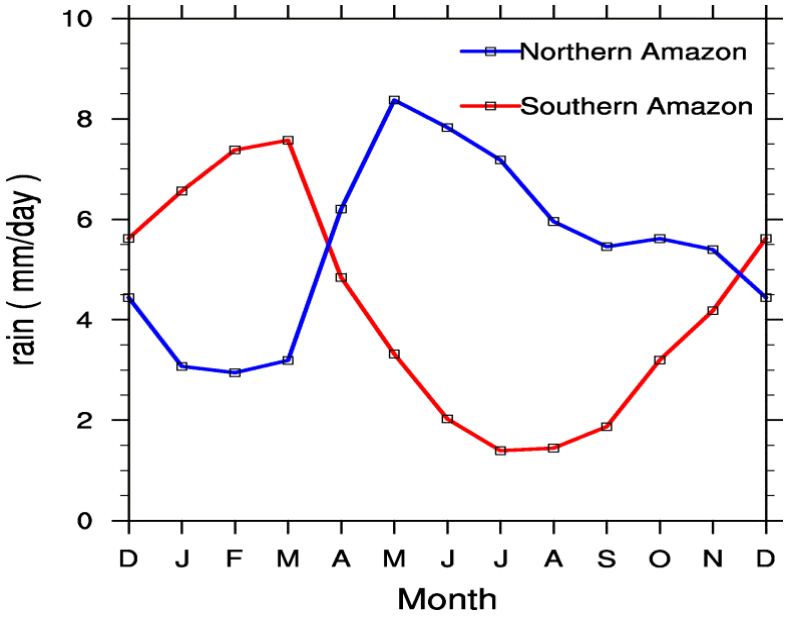


Figure 19: Longitude-averaged rain rate in the Amazon from the Global Precipitation Climatology Project (GPCP) dataset.

The other possibility is associated with the seasonal cycle of plant phenology. Site level measurements show the photosynthesis of plants in the Amazon increases during dry seasons [59]. The dry season has less rain but offers more solar radiation, plus water is not limited in this region, so plants have better conditions for photosynthetic activities resulting in a higher FPAR value for light-rich dryer days.

### 4.6 Conclusion and Summary

Our findings show that the model roughly agrees with observations in the seasonal cycle and spatial patterns but does not reproduce the diurnal cycle or long-term trends. Discrepancies also exist in seasonality magnitudes, peak value months and spatial heterogeneity. Though FPAR is a key representative parameter for the solar radiation partitioning scheme, its accuracy is also decided by input data such as

leaf area index (LAI) and other conditions. Therefore we analyzed possible reasons for disagreements and then focused on those potentially related to the land surface solar radiation partitioning scheme (i.e., spatial patterns of peak month in the Amazon and diurnal cycle). We identified the discrepancy in the diurnal cycle as due to the absence of dependence on sun angle in the model. Implementation of sun angle dependence in a one-dimensional (1-D) model is proposed. The need for better relating vegetation to climate in the model indicated by long-term trends is also noted. Evaluation of the CLM4 land surface solar radiation partitioning scheme using remote sensing and site level FPAR datasets provides targets for future development in its representation of this naturally complicated process.

# Chapter 5: Concluding Remarks and Future Works

This study evaluates CLM4 FPAR with both remotely sensed FPAR products and flux tower observations. Seasonal cycle, diurnal cycle, long-term trends and spatial patterns are employed to investigate differences of FPAR between CLM4 and observations. The objective is to offer guidance for future developments in the CLM4 land surface solar radiation partitioning scheme.

Our findings show that CLM4 simulation and satellite observations are in broad agreement with seasonal cycle, long-term trends and zonal spatial patterns. These three variables are primarily determined by plant phenology, such as LAI, and therefore should be mostly accredited to the CN module. Some discrepancies still exist. For example, CLM4 has a systematically weaker seasonality; large bias in seasonality was found in certain PFT types. We found similar discrepancies between CLM4 LAI and GIMMS LAI3g. Since LAI is the primary input for FPAR calculation, these discrepancies between the model and satellite observations might be addressed through the improvement of LAI parameterization in CLM4.

Our study highlights the need for treatment of sun angle effect in the FPAR diurnal cycle in CLM. The model currently has plants and bare soil separately allocated into different patches so the plant becomes “shadowless”: the soil between canopies would never be blocked from solar radiation by the canopy since it is in another patch. Based on the boundary conditions from the Boolean Scene Model, a possible solution for this problem is proposed and illustrated with a two-element model that is simplified from the CLM4 land surface scheme. We also tried to explain the spatial patterns of peak FPAR months in the Amazon, but tropical rainfall forest might be too dense to be sensitive to the angular effect. In addition, two other possibilities (i.e., cloud contamination and higher photosynthesis in dry seasons) could also explain the phenomenon.

We also note with particular interest that the CLM4 simulations generally reproduced the increasing trend that inferred from the GIMMS3g data sets for both FPAR and LAI but with smaller significance levels. GIMMS3g data illustrates extensively significant increasing trends in several transitional eco-regions, which indicates influences of forcing factor changes on plant phenology. The model, however, has only limited grids exceeding the 90% significance level though it reproduces the trends over many different areas. A target (i.e., climate-vegetation relations) was hence noted for CLM4 future development.

As mentioned, the GIMMS3g dataset has an over 30-year availability, consists of NDVI, LAI and FPAR estimations and thus offers a unique opportunity for climate model evaluation, especially for long-term changes. Various factors contribute to the vegetation inter-annual changes, such as precipitation, atmospheric $CO_2$ concentration and aerosol. Their relations to vegetation could be established by the GIMMS3g dataset, be used to identify the deficiencies in the CLM4's long-term trend simulation and eventually contribute to CLM4 future development.

## References


1. Dickinson, R. E. Land Surface Processes and Climate--Surface Albedos and Energy Balance. *Theory of Climate Proceedings of a Symposium Commemorating the TwoHundredth Anniversary of the Academy of Sciences of Lisbon* **1983**, *25*, 305–353.

2. Avissar, R.; Verstraete, M. M. The representation of continental surface processes in atmospheric models. *Reviews of Geophysics* **1990**, *28*, 35–52.

3. Sellers, P. J.; Dickinson, R. E.; Randall, D. A.; Betts, A. K.; Hall, F. G.; Berry, J. A.; Collatz, G. J.; Denning, A. S.; Mooney, H. A.; Nobre, C. A.; Sato, N.; Field, C. B.; Henderson-Sellers, A. Modeling the Exchanges of Energy, Water, and Carbon Between Continents and the Atmosphere. *Science* **1997**, *275*, 502–509.

4. Viterbo, P.; Betts, A. K. Impact on ECMWF forecasts of changes to the albedo of the boreal forests in the presence of snow. *Journal of Geophysical Research* **1999**, *104*, 27803–27810.

5. Ma, Y.; Su, Z.; Koike, T.; Yao, T.; Ishikawa, H.; Ueno, K.; Menenti, M. On measuring and remote sensing surface energy partitioning over the Tibetan Plateau—from GAME/Tibet to CAMP/Tibet. *Physics and Chemistry of the Earth, Parts A/B/C* **2003**, *28*, 63–74.

6. Gu, L.; Meyers, T.; Pallardy, S. G.; Hanson, P. J.; Yang, B.; Heuer, M.; Hosman, K. P.; Riggs, J. S.; Sluss, D.; Wullschleger, S. D. Direct and indirect effects of atmospheric conditions and soil moisture on surface energy partitioning revealed by a prolonged drought at a temperate forest site. *Journal of Geophysical Research* **2006**, *111*, 1–13.

7. Li, S.-G.; Eugster, W.; Asanuma, J.; Kotani, A.; Davaa, G.; Oyunbaatar, D.; Sugita, M. Energy partitioning and its biophysical controls above a grazing steppe in central Mongolia. *Agricultural and Forest Meteorology* **2006**, *137*, 89–106.

8. Betts, A. K.; Ball, J. H.; Beljaars, A. C. M.; Miller, M. J.; Viterbo, P. A. The land surface-atmosphere interaction: A review based on observational and global modeling perspectives. *Journal of Geophysical Research* **1996**, *101*, 7209–7225.

9. Baldocchi, D. D.; Law, B. E.; Anthoni, P. M. On measuring and modeling energy fluxes above the floor of a homogeneous and heterogeneous conifer forest. *Agricultural and Forest Meteorology* **2000**, *102*, 187–206.

10. Dickinson, R. E.; Zhou, L.; Tian, Y.; Liu, Q.; Lavergne, T.; Pinty, B.; Schaaf, C. B.; Knyazikhin, Y. A three-dimensional analytic model for the scattering of a spherical bush. *Journal of Geophysical Research* **2008**, *113*, D20113.

11. Pinty, B.; Lavergne, T.; Kaminski, T.; Aussedat, O.; Giering, R.; Gobron, N.; Taberner, M.; Verstraete, M. M.; Vo□beck, M.; Widlowski, J.-L. Partitioning the solar radiant fluxes in forest canopies in the presence of snow. *Journal of Geophysical Research* **2008**, *113*, D04104.

12. Guan, H.; Wilson, J. L. A hybrid dual-source model for potential evaporation and transpiration partitioning. *Journal of Hydrology* **2009**, *377*, 405–416.

13. Pinty, B.; Lavergne, T.; Dickinson, R. E.; Widlowski, J. L.; Gobron, N.; Verstraete, M. M. Simplifying the interaction of land surfaces with radiation for relating remote sensing products to climate models. *Journal of Geophysical Research* **2006**, *111*, D02116.

14. Bonan, G. B.; Lawrence, P. J.; Oleson, K. W.; Levis, S.; Jung, M.; Reichstein, M.; Lawrence, D. M.; Swenson, S. C. Improving canopy processes in the Community Land Model version 4 (CLM4) using global flux fields empirically inferred from FLUXNET data. *Journal of Geophysical Research* **2011**, *116*, 1–22.

15. Oleson, K. W.; Lawrence, D. M.; Gordon, B.; Flanner, M. G.; Kluzek, E.; Peter, J.; Levis, S.; Swenson, S. C.; Thornton, E.; Feddema, J. Technical description of version 4.0 of the Community Land Model (CLM). **2010**.

16. Niu, G.-Y.; Yang, Z.-L. Effects of vegetation canopy processes on snow surface energy and mass balances. *Journal of Geophysical Research* **2004**, *109*, D23111.

17. Bonan, G. B.; Levis, S.; Kergoat, L.; Oleson, K. W. Landscapes as patches of plant functional types: An integrating concept for climate and ecosystem models. *Global Biogeochemical Cycles* **2002**, *16*, 1021.

18. Tian, Y.; Dickinson, R. E.; Zhou, L.; Zeng, X.; Dai, Y.; Myneni, R. B.; Knyazikhin, Y.; Zhang, X.; Friedl, M.; Yu, H.; Wu, W.; Shaikh, M. Comparison of seasonal and spatial variations of leaf area index and fraction of absorbed photosynthetically active radiation from Moderate Resolution Imaging Spectroradiometer (MODIS) and Common Land Model. *Journal of Geophysical Research* **2004**, *109*, D01103.

19. Senna, M. C. A.; Costa, M. H.; Shimabukuro, Y. E. Fraction of photosynthetically active radiation absorbed by Amazon tropical forest: A comparison of field measurements, modeling, and remote sensing. *Journal of Geophysical Research* **2005**, *110*, G01008.

20. Gobron, N.; Pinty, B.; Aussedat, O.; Chen, J. M.; Cohen, W. B.; Fensholt, R.; Gond, V.; Huemmrich, K. F.; Lavergne, T.; Mélin, F.; Privette, J. L.; Sandholt, I.; Taberner, M.; Turner, D. P.; Verstraete, M. M.; Widlowski, J.-L. Evaluation of fraction of absorbed photosynthetically active radiation products for different canopy

radiation transfer regimes: Methodology and results using Joint Research Center products derived from SeaWiFS against ground-based estimations. *Journal of Geophysical Research* **2006**, *111*.

21. Gobron, N.; Pinty, B.; Aussedat, O.; Taberner, M.; Faber, O.; Melin, F.; Lavergne, T.; Robustelli, M.; Snoeij, P. Uncertainty estimates for the FAPAR operational products derived from MERIS — Impact of top-of-atmosphere radiance uncertainties and validation with field data. *Remote Sensing of Environment* **2008**, *112*, 1871–1883.

22. Steinberg, D. C.; Goetz, S. J.; Hyer, E. J. Validation of MODIS FPAR products in boreal forests of Alaska. *IEEE Transactions on Geoscience and Remote Sensing* **2006**, *44*, 1818–1828.

23. Huemmrich, K. F.; Privette, J. L.; Mukelabai, M.; Myneni, R. B.; Knyazikhin, Y. Time□series validation of MODIS land biophysical products in a Kalahari woodland, Africa. *International Journal of Remote Sensing* **2005**, *26*, 4381–4398.

24. Levis, S.; Bonan, G.; Vertenstein, M.; Oleson, K. *The Community Land Model's Dynamic Global Vegetation Model (CLM-DGVM): Technical description and user's guide*; University Corporation for Atmospheric Research, 2004.

25. McCallum, I.; Wagner, W.; Schmullius, C.; Shvidenko, A.; Obersteiner, M.; Fritz, S.; Nilsson, S. Comparison of four global FAPAR datasets over Northern Eurasia for the year 2000. *Remote Sensing of Environment* **2010**, *114*, 941–949.

26. Knyazikhin, Y.; Martonchik, J. V; Myneni, R. B.; Diner, D. J.; Running, S. W. Synergistic algorithm for estimating vegetation canopy leaf area index and fraction of absorbed photosynthetically active radiation from MODIS and MISR data. *Journal of Geophysical Research* **1998**, *103*, 32257–32275.

27. Gobron, N.; Pinty, B.; Mélin, F.; Taberner, M.; Verstraete, M. M.; Robustelli, M.; Widlowski, J. L. Evaluation of the MERIS/ENVISAT FAPAR product. *Advances in Space Research* **2007**, *39*, 105–115.

28. Weiss, M.; Baret, F.; Garrigues, S.; Lacaze, R. LAI and fAPAR CYCLOPES global products derived from VEGETATION. Part 2: validation and comparison with MODIS collection 4 products. *Remote Sensing of Environment* **2007**, *110*, 317–331.

29. Zhang, Q.; Xiao, X.; Braswell, B. Characterization of seasonal variation of forest canopy in a temperate deciduous broadleaf forest, using daily MODIS data. *Remote Sensing of Environment* **2006**, *105*, 189–203.

30. Ollinger, S.; Smith, M.-L. Net Primary Production and Canopy Nitrogen in a Temperate Forest Landscape: An Analysis Using Imaging Spectroscopy, Modeling and Field Data. *Ecosystems* **2005**, *8*, 760–778.

31. Myneni, R.; Hoffman, S.; Knyazikhin, Y.; Privette, J.; Glassy, J.; Tian, Y.; Wang, Y.; Song, X.; Zhang, Y.; Smith, G.; Lotsch, A.; Friedl, M.; Morisette, J.; Votava, P.; Nemani, R.; Running, S. Global products of vegetation leaf area and fraction absorbed PAR from year one of MODIS data. *Remote Sensing of Environment* **2002**, *83*, 214–231.

32. Zhao, M.; Heinsch, F. A.; Nemani, R. R.; Running, S. W. Improvements of the MODIS terrestrial gross and net primary production global data set. *Remote Sensing of Environment* **2005**, *95*, 164–176.

33. Samanta, A.; Costa, M. H.; Nunes, E. L.; Vieira, S. A.; Xu, L.; Myneni, R. B. Comment on "Drought-Induced Reduction in Global Terrestrial Net Primary Production from 2000 Through 2009". *Science* **2011**, *333*, 1093–1093.

34. Yuan, H.; Dai, Y.; Xiao, Z.; Ji, D.; Shangguan, W. Reprocessing the MODIS Leaf Area Index products for land surface and climate modelling. *Remote Sensing of Environment* **2011**, *115*, 1171–1187.

35. Zhu, Z.; Bi, J.; Pan, Y.; Ganguly, S.; Samanta, A.; Xu, L.; Anav, A.; Nemani, R. R.; Myneni, R. B. Global Data Sets of Vegetation LAI3g and FPAR3g derived from GIMMS NDVI3g for the period 1981 to 2011. *Remote Sensing*.

36. Myneni, R. B.; Ramakrishna, R.; Nemani, R.; Running, S. W. Estimation of global leaf area index and absorbed par using radiative transfer models. *IEEE Transactions on Geoscience and Remote Sensing* **1997**, *35*, 1380–1393.

37. Gobron, N.; Mélin, F.; Pinty, B.; Verstraete, M. M.; Widlowski, J.-L.; Bucini, G. A global vegetation index for SeaWiFS: Design and applications. In *Remote Sensing and Climate Modeling: Synergies and Limitations SE - 1*; Beniston, M.; Verstraete, M., Eds.; Springer Netherlands, 2003; Vol. 7, pp. 5–21.

38. Gobron, N.; Belward, a.; Pinty, B.; Knorr, W. Monitoring biosphere vegetation 1998–2009. *Geophysical Research Letters* **2010**, *37*, 1–6.

39. Pinty, B.; Gobron, N.; Melin, F.; Verstraete, M. *A Time Composite Algorithm for FAPAR Products: Theoretical Basis Document*; 2002; pp. 1–8.

40. Fensholt, R.; Sandholt, I.; Rasmussen, M. S. Evaluation of MODIS LAI, fAPAR and the relation between fAPAR and NDVI in a semi-arid environment using in situ measurements. *Remote Sensing of Environment* **2004**, *91*, 490–507.

41. Fritsch, S.; Machwitz, M.; Ehammer, A.; Conrad, C.; Dech, S. Validation of the collection 5 MODIS FPAR product in a heterogeneous agricultural landscape in arid Uzbekistan using multitemporal RapidEye imagery. *International Journal of Remote Sensing* **2012**, 6818–6837.

42. Randerson, J. T.; Hoffman, F. M.; Thornton, P. E.; Mahowald, N. M.; Lindsay, K.; Lee, Y.-H.; Nevison, C. D.; Doney, S. C.; Bonan, G.; Stöckli, R.; Covey, C.; Running, S. W.; Fung, I. Y. Systematic assessment of terrestrial biogeochemistry in coupled climate-carbon models. *Global Change Biology* **2009**, *15*, 2462–2484.

43. Strahler, A.; Jupp, D. Modeling bidirectional reflectance of forests and woodlands using Boolean models and geometric optics. *Remote Sensing of Environment* **1990**, *166*, 153–166.

44. Peng, D.; Zhang, B.; Liu, L.; Fang, H.; Chen, D. Characteristics and drivers of global NDVI-based FPAR from 1982 to 2006. *Global Biogeochemical Cycles* **2012**, *26*, 1–15.

45. Thornton, P. E.; Zimmermann, N. E. An Improved Canopy Integration Scheme for a Land Surface Model with Prognostic Canopy Structure. *Journal of Climate* **2007**, *20*, 3902–3923.

46. Thornton, P. E.; Law, B. E.; Gholz, H. L.; Clark, K. L.; Falge, E.; Ellsworth, D. S.; Goldstein, A. H.; Monson, R. K.; Hollinger, D.; Falk, M. Modeling and measuring the effects of disturbance history and climate on carbon and water budgets in evergreen needleleaf forests. *Agricultural and forest meteorology* **2002**, *113*, 185–222.

47. Thornton, P. E.; Rosenbloom, N. A. Ecosystem model spin-up: Estimating steady state conditions in a coupled terrestrial carbon and nitrogen cycle model. *Ecological Modelling* **2005**, *189*, 25–48.

48. Shi, X.; Mao, J.; Thornton, P. E.; Hoffman, F. M.; Post, W. M. The impact of climate, $CO_2$, nitrogen deposition and land use change on simulated contemporary global river flow. *Geophysical Research Letters* **2011**, *38*, L08704.

49. Mao, J. .; Shi, X. .; Thornton, P. E. .; Hoffman, F. M. .; Zhu, Z. .; Myneni, R. B. Global latitudinal-asymmetric vegetation growth trends and their driving mechanisms: 1982-2009. *Remote Sensing* **2013**.

50. Lawrence, P. J.; Chase, T. N. Representing a new MODIS consistent land surface in the Community Land Model (CLM 3.0). *Journal of Geophysical Research* **2007**, *112*, doi:10.1029/2006JG000168.

51. Mao, J.; Thornton, P.; Shi, X. Remote Sensing Evaluation of CLM4 GPP for the Period 2000-09. *Journal of Climate* **2012**, 5327–5342.

52. Heil, G. W.; Muys, B.; Hansen, K. *Environmental effects of afforestation in North-Western Europe: from field observations to decision support*; Springer, 2007; Vol. 1.

53. Huber, S.; Fensholt, R. Analysis of teleconnections between AVHRR-based sea surface temperature and vegetation productivity in the semi-arid Sahel. *Remote Sensing of Environment* **2011**, *115*, 3276–3285.

54. Pinzon, H. E. E. and M. K. R. and D. A. W. and U. S. B. and C. J. T. and J. E. Dynamics of aboveground phytomass of the circumpolar Arctic tundra during the past three decades. *Environmental Research Letters* **2012**, *7*, 15506.

55. Tape, K.; Sturm, M.; Racine, C. The evidence for shrub expansion in Northern Alaska and the Pan-Arctic. *Global Change Biology* **2006**, *12*, 686–702.

56. Zeng, H.; Jia, G.; Epstein, H. Recent changes in phenology over the northern high latitudes detected from multi-satellite data. *Environmental Research Letters* **2011**, *045508*.

57. Walker, D. a; Epstein, H. E.; Raynolds, M. K.; Kuss, P.; Kopecky, M. a; Frost, G. V; Daniëls, F. J. a; Leibman, M. O.; Moskalenko, N. G.; Matyshak, G. V; Khitun, O. V; Khomutov, a V; Forbes, B. C.; Bhatt, U. S.; Kade, a N.; Vonlanthen, C. M.; Tichý, L. Environment, vegetation and greenness (NDVI) along the North America and Eurasia Arctic transects. *Environmental Research Letters* **2012**, *7*, 015504.

58. Dickinson, R. E. Determination of the multi-scattered solar radiation from a leaf canopy for use in climate models. *Journal of Computational Physics* **2008**, *227*, 3667–3677.

59. Saleska, S. R.; Miller, S. D.; Matross, D. M.; Goulden, M. L.; Wofsy, S. C.; Da Rocha, H. R.; De Camargo, P. B.; Crill, P.; Daube, B. C.; De Freitas, H. C.; Hutyra, L.; Keller, M.; Kirchhoff, V.; Menton, M.; Munger, J. W.; Pyle, E. H.; Rice, A. H.; Silva, H. Carbon in Amazon forests: unexpected seasonal fluxes and disturbance-induced losses. *Science* **2003**, *302*, 1554–1557.

# Vita

Kai Wang was born in Yueyang, Hunan, China. He earned his B.S. in Cartography and Geographic Information Science and his B.A. in Economics from Peking University in 2007. Kai then went on to receive his M.S. in Remote Sensing at the Institute of Remote Sensing and Digital Earth, Chinese Academy of Sciences in 2010. He began his graduate studies in geological sciences in the Jackson School of Geosciences at the University of Texas at Austin in 2010.

Permanent address: kaiwang@utexas.edu

This thesis was typed by the author.